nature communications

Article

https://doi.org/10.1038/s41467-025-63377-3

Reprogramming the tumor microenvironment with c-MYC-based gene circuit platform to enhance specific cancer immunotherapy

Received: 19 December 2024

Accepted: 18 August 2025

Published online: 27 August 2025

Check for updates

Hengji Zhan[1,2,3,6], Hongjin Wang[1,2,3,6], Bolin Pan[1,2,3,6], Junlin Lu[1,2,3,6], Kanghua Xiao[1,2,4,6], Jiajian Lai[1,2,3], Zehua Chen[1,2,3], Kaiwen Jie[1,2,3], Siting Chen[1,2,3], Hong Li[5], Tianxin Lin[1,2,3] ✉ & Xu Chen[1,2,3] ✉

Intratumor heterogeneity (ITH) is associated with anti-tumoral immune response and with the efficiency of cancer immunotherapy, yet overcoming ITH remains a significant challenge. Notably, cellular MYC (c-MYC) has been shown to be a pivotal orchestrator of this ITH progression. Here, we develop a c-MYC-based sensing circuit (cMSC) that is activated exclusively by aberrant c-MYC levels, along with an exosome-based cell-to-cell (CtC) system that augments communication among tumor cells, effectively targeting all cells in tumors circumventing the limitations imposed by ITH. Further expression of multifunctional immunostimulatory agents in these cMSC-reprogrammed cancer cells remodels the tumor microenvironment, enhancing selective T-cell-mediated oncolysis. Our cMSC/CtC platform specifically senses aberrant c-MYC expression and subsequently triggers a robust cancer immunotherapeutic response. These findings offer a promising avenue for targeting cancers via precisely sensing c-MYC, overcoming the limitations of ITH.

Immunotherapy has achieved great clinical success in many types of cancer, yet a large proportion of patients with cancer, especially those with solid tumors, do not benefit from it. Moreover, the determinants of cancer immunotherapy efficacy remain largely unknown[1]. A leading hypothesis in the immunotherapy field is intratumor heterogeneity (ITH), manifested by a diverse distribution of clonal and subclonal mutations and neoantigens[2,3], which may affect immune surveillance[4–6]. In addition, ITH is crucially involved in resistance to therapy, metastasis and cancer relapse, yet overcoming ITH is still a major challenge[7–9].

Although ITH is a complex biological process and difficult to predict, some important factors, such as cellular MYC (c-MYC), change in expression as tumor cells progress through ITH, contributing to the diverse phenotypes observed within a tumor[10]. c-MYC is a highly heterogeneously expressed transcription factor that serves as a pivotal orchestrator of transcriptional and phenotypic diversity in cancer[10,11]. The overexpression of c-MYC, which serves as a central oncogene in most tumors, leads to cancer progression and poor prognosis[12–16]. Many efforts have been devoted to interfering with c-MYC function

[1]Department of Urology, Sun Yat-sen Memorial Hospital, Sun Yat-sen University, Guangzhou, China. [2]Guangdong Provincial Key Laboratory of Malignant Tumor Epigenetics and Gene Regulation, Guangdong-Hong Kong Joint Laboratory for RNA Medicine, Sun Yat-Sen Memorial Hospital, Sun Yat-Sen University, Guangzhou, China. [3]Guangdong Provincial Clinical Research Center for Urological Diseases, Guangzhou, China. [4]Guangdong Provincial Key Laboratory of Urology, Guangzhou Institute of Urology, Department of Urology, The First Affiliated Hospital of Guangzhou Medical University, Guangzhou Medical University, Guangzhou, China. [5]BioMed Laboratory, Guangzhou Jingke Biotech Group, Guangzhou, China. [6]These authors contributed equally: Hengji Zhan, Hongjin Wang, Bolin Pan, Junlin Lu, Kanghua Xiao. ✉e-mail: lintx@mail.sysu.edu.cn; chenx457@mail.sysu.edu.cn

directly in tumor cells[17,18]. However, simple inhibition of high c-MYC-expressing cells fails to kill all cancer cells due to the escape of low c-MYC-expressing cells. In addition, indiscriminately inhibiting MYC transcriptional mechanisms by targeting cofactors such as MAX, CDKs and BRD4, USPs, or PLK1 has shown limited success and can cause severe side effects. Functionally, c-MYC plays physiological and pathological roles by selectively binding to target promoters[14,19–21]. The value of c-MYC as a therapeutic target remains largely unexplored, primarily owing to difficulties in discerning pathological from physiological c-MYC expression. Therefore, there are still massive challenges in the development of effective and selective anticancer therapies that target c-MYC.

Compared with specific gene-targeted therapies for inhibiting c-MYC, cancer immunotherapy has emerged as a promising approach for the treatment of diverse cancer types[22]. However, several major challenges limit the promotion of cancer immunotherapy, including tumor-mediated immunosuppression, particularly the lack of specific cell-surface antigens. These challenges are caused mainly by ITH, which impedes further clinical application of cancer immunotherapy[23,24]. In particular, high c-MYC expression in cancer cells has been shown to cause immune evasion and immunotherapy failure through the modulation of immune regulatory molecules[25,26]. Chimeric antigen receptor T (CAR-T) cells[27] and bispecific antibodies[28] provide a viable strategy for targeted cancer immunotherapy, but they are ineffective in cancers without highly specific tumor cell-surface antigens and ITH[29]. Some synthetic T-cell engagers (STEs) are expressed on the surfaces of tumor cells to solve the problem of contact between cancer cells and T cells; however, it is difficult to express STE specifically in all cancer cells because of ITH.

To address the challenge of intratumoral heterogeneity (ITH), we have classified the tumor cell population into two distinct categories: cells with high levels of c-MYC expression (MYC^{high}) and those with low levels of c-MYC expression (MYC^{low}). We hypothesize that a c-MYC–inducible genetic circuit is activated specifically when c-MYC expression surpasses a certain threshold, thereby facilitating the expression of multiple immune modulators in MYC^{high} cells. This design would also reprogram cell–cell communication, allowing for the expression of immune modulators in MYC^{low} tumor cells. Here, we characterized a gene circuit platform capable of specifically sensing aberrant c-MYC expression, subsequently initiating robust cancer immunotherapy without the limitations of ITH. This strategy encompasses a cMSC activated exclusively by anomalous c-MYC levels paired with the CtC system, which augments intertumor-to-tumor cell communication, effectively addressing the challenges of ITH. Remarkably, the cMSC reprogrammed cancer cells expressing immunostimulatory agents to trigger selective T-cell-mediated oncolysis. In combination with the CtC system, this approach overcame ITH therapeutic challenges, enhancing the efficacy of immunotherapeutic tumor ablation both in vitro and in vivo. Efficacy assays employing orthotopic xenograft models of bladder cancer treated with an AAV-delivered cMSC/CtC platform confirmed both tumor clearance and prolonged survival. Overall, our programmable immunoregulatory gene circuit based on c-MYC expression recognition has a wide range of potential uses in precise cancer therapy without limitations associated with ITH (Fig. 1).

Results

The design of a c-MYC-based platform to overcome the limitations of ITH

The c-MYC protein is overexpressed in most cancers, especially in bladder cancer (Supplementary Fig. 1a). The expression of c-MYC was strongly associated with ITH in tumors, including bladder, lung, and liver cancers (Supplementary Fig. 1b). Notably, increased expression and heterogeneity of c-MYC were detected in patients with advanced-stage and advanced-grade bladder cancer and were positively correlated (Supplementary Fig. 1c–f). In addition, high expression of c-MYC has been detected in various molecular subtypes of bladder cancer, particularly in the basal/squamous (Ba/Sq) subtype, which is the most aggressive and has the worst prognosis among bladder cancer subtypes (Supplementary Fig. 2a). We also found that the progression of this bladder cancer subtype is highly correlated with c-MYC expression (Supplementary Fig. 2b, c). Notably, increased expression and heterogeneity of c-MYC were found to be positively correlated with c-MYC expression (Supplementary Fig. 2d, e). On this basis, we developed a strategy for overcoming the limitations of ITH reported here through reprogramming cancer cells via a c-MYC-based gene circuit platform.

This approach relies on two arms. First, we constructed an autoregulatory gene circuit activated only by high expression of c-MYC in cells. Specifically, a synthetic c-MYC-activated promoter (P_{aMYC}) was used to drive the expression of genes of interest (GOIs). A synthetic c-MYC-repressed promoter (P_{rMYC}) was subsequently used to express a de novo reengineered artificial RNA that antagonizes the expression of GOIs driven by P_{aMYC}. Owing to this bidirectional interaction between P_{aMYC} and P_{rMYC}, only c-MYC expression levels above a specific threshold can activate the cMSC to express GOIs. Second, we used the cMSC to express CtC components and therapeutic genes. cMSC-transfected cancer cells with MYC^{high} produce exosomes that are directed toward cancer cells with MYC^{low}. In this process, the engineered exosomes shuttle the target mRNAs of the therapeutic genes from MYC^{high} cancer cells to MYC^{low} cancer cells for translation. Through this approach, we enabled the expression of therapeutic genes across all types of tumor cells, thereby overcoming the limitations of ITH (Fig. 1).

cMSC design and implementation

We generated P_{aMYC} from known c-MYC-binding motifs[30] and encoded multiple binding motifs in tandem upstream of the synthetic core promoter[31]. P_{aMYC} was used to drive the expression of green fluorescent protein (GFP) to test its specificity and activity in 293T cells with different c-MYC expression levels. To characterize the efficiency and specificity of P_{aMYC}, we used the CMV promoter (P_{CMV}) to drive the expression of blue fluorescent protein (BFP) and inserted it upstream of P_{aMYC} expressing GFP (P_{aMYC}-GFP) in the same expression vector as a label for transfected cells (Fig. 2a). We transfected P_{aMYC}-GFP into 293T cells with different c-MYC expression levels and used fluorescence-activated cell sorting (FACS) for quantitative analysis. We gated BFP^+ cells to determine the efficiency of P_{aMYC}, given that every BFP^+ cell has the potential to express GFP. The transfection of P_{aMYC}-GFP resulted in only 5.9-fold greater activation of GFP expression in MYC^{high} than in MYC^{low} (Fig. 2c and Supplementary Fig. 3a). Notably, P_{aMYC} exhibited nonnegligible unwanted background expression in MYC^{low} cells. To ensure that the GOIs are expressed only in MYC^{high} cells, the background expression of GOIs in MYC^{low} cells should be eliminated. Therefore, we sought to use a smart inhibition strategy to eliminate unwanted background expression in MYC^{low}. Ideally, the inhibition of GOIs in MYC^{low} should be strong enough to eliminate background expression, whereas the inhibition of GOIs should be as weak as possible to allow more expression of GOIs in MYC^{high}. Therefore, we introduced the synthetic c-MYC-repressed promoter (P_{rMYC}), whose activity was negatively correlated with c-MYC expression, as an inhibitory tool to partially suppress the GOI expression driven by P_{aMYC}. In the construction of PrMYC, we characterized the core transcriptional elements of candidate promoters and identified negative regulatory motifs mediated by c-MYC[32]. Compared with that in MYC^{low} cells, the P_{rMYC}-driven expression of mCherry in MYC^{high} cells was 2.6-fold lower (Fig. 2b, c and Supplementary Fig. 3a–c).

Next, we used P_{rMYC} as a highly effective transcriptional inhibitory tool against the expression of GOIs driven by P_{aMYC} and constructed a c-MYC-based sensing circuit (cMSC). To avoid crosstalk between other endogenous cellular components and the gene circuits we designed,

we constructed a ribozyme-based mRNA degradation system with high specificity and inhibition efficiency for target mRNAs. Hammerhead ribozymes, a class of small self-cleaving ribozymes with fast cleavage kinetics, are widely used as effector domains for RNA switching. The introduction of these most potent ribozymes in the 3′ untranslated region (UTR) of the reporter gene causes the mRNA to degrade rapidly, preventing translation[33,34]. Here, based on a potent ribozyme[34], we developed an mRNA degradation system mediated by a ribozyme catalytic self-cleavage reaction to inhibit target mRNA translation. First, we analyzed the composition of the ribozyme system. In the ribozyme, the stabilization of stems I, II, and III is critical for maintaining the catalytic activity of the ribozyme (Supplementary Fig. 4a). Among them, the tertiary interaction between loop II and the bulge of stem I greatly increases hammerhead ribozyme activity[35]. Based on these characteristics, we divided the ribozyme into two independent parts (split-ribozyme-1 and split-ribozyme-2) from stem I to stem III (Supplementary Fig. 4b). With the help of the catalytic core box of the ribozyme, which is expected to achieve highly specific degradation of the target mRNA, we systematically validated and optimized various aspects of split-ribozyme-1/split-ribozyme-2 and described how the sequence and composition of split-ribozyme-1/split-ribozyme-2 affect the efficiency of this system (Supplementary Fig. 4c–i).

In the proof-of-principle construction of the preliminary cMSC, P_{aMYC} was used to drive the expression of GFP, whose expression encoding cassette was reengineered with split-ribozyme-1 in tandem, and P_{rMYC} was used to drive the expression of split-ribozyme-2, which matched split-ribozyme-1 to cleave the mRNA of GFP specifically, serving as a preliminary cMSC-GFP (Fig. 2d). All the above components were constructed in the same vector. To characterize cMSC efficiency quantitatively, we inserted a P_{CMV}-BFP sequence upstream of the preliminary cMSC-GFP region, which functions as a marker of transfected cells. We transfected this preliminary cMSC-GFP vector into 293T cells with different c-MYC expression levels and used FACS for quantitative analysis. In the MYC^{low} cells, preliminary cMSC-GFP vector transfection

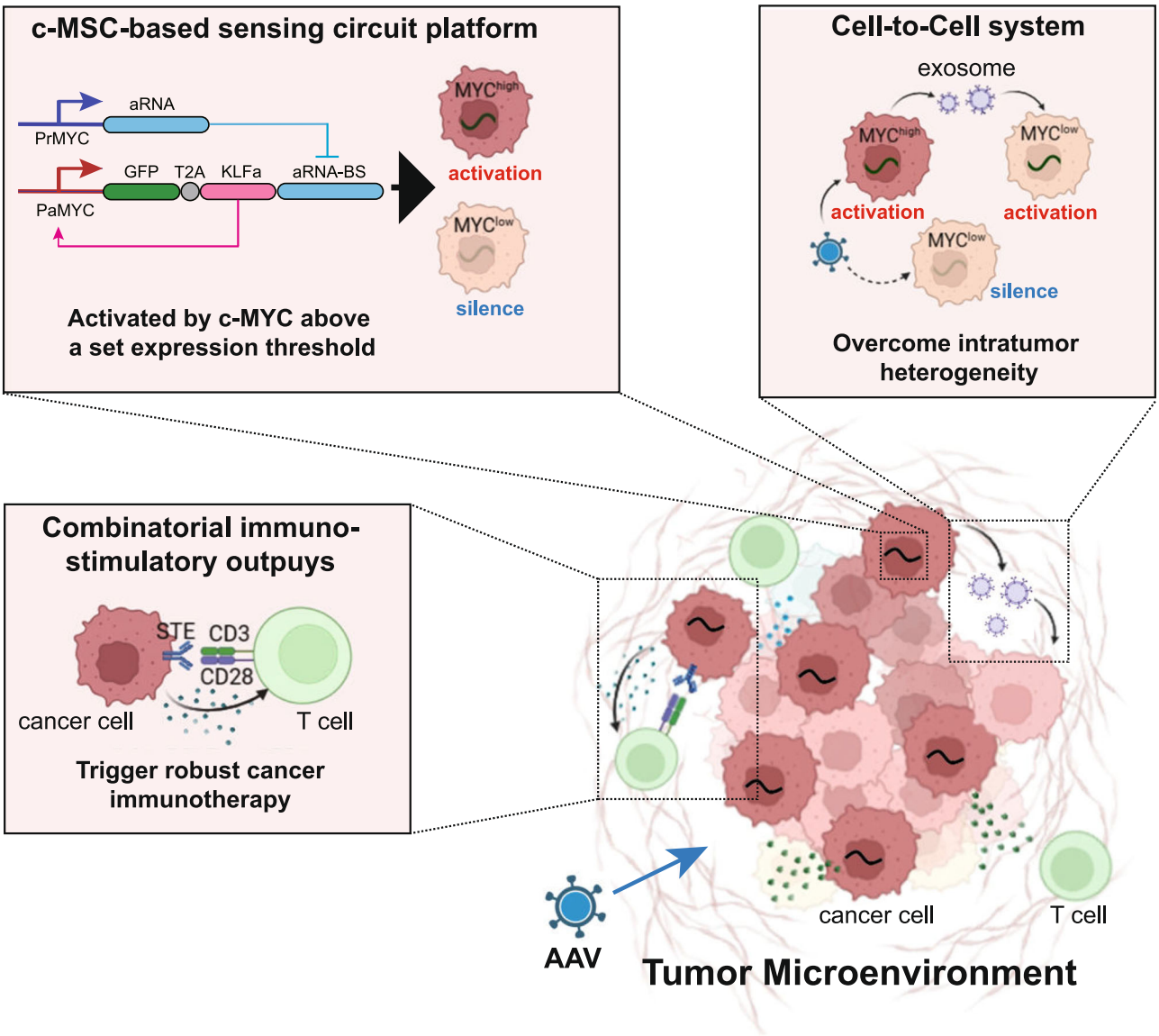

Fig. 1 | Construction of a c-MYC-based gene circuit for reprogramming cancer cells to trigger specific cancer immunotherapies. Overall design of the gene circuit platform. An intravesical instillation therapy based on the cMSC/CtC platform has been delivered by AAV and developed to eradicate bladder cancer. The cMSC is programmed to be activated precisely in cancer cells with pathological c-MYC expression. The cell-to-cell system is designed to augment gene circuit communication in tumor cells. Combinatorial immunostimulatory outputs, including STE bitargeting CD3 and CD28, IL-21, CCL5, and anti-PD1, are expressed by the cMSC/CtC platform to selectively trigger robust cancer immunotherapy. Created in BioRender. Zhan, H. (2025) https://BioRender.com/3egw3g5.

https://doi.org/10.1038/s41467-025-63377-3

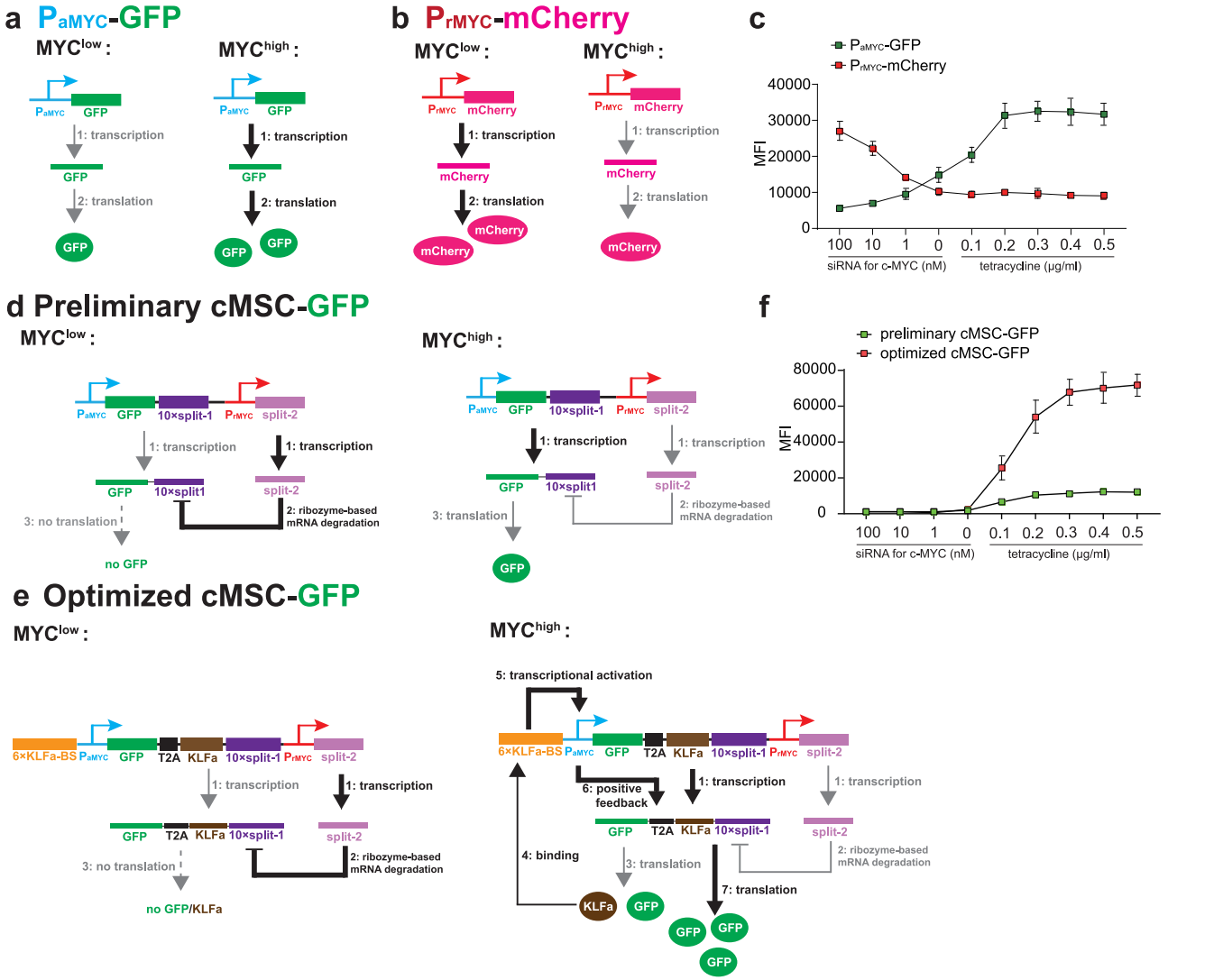

Fig. 2 | Design and implementation of the cMSC. a Schematic showing synthetic P_{aMYC} expressing GFP in MYC^{low} and MYC^{high} cells. P_{aMYC} exhibited low transcriptional activity in MYC^{low} cells but high activity in MYC^{high} cells. **b** Schematic illustration of synthetic P_{rMYC} expressing mCherry across c-MYC expression gradients. P_{rMYC} exhibited high transcriptional activity in MYC^{low} cells but low activity in MYC^{high} cells. **c** Mean fluorescence intensity (MFI) of GFP- and mCherry-driven expression of P_{aMYC} and P_{rMYC} in BFP^+ cells, respectively, over a range of siRNA and tetracycline concentrations. The data are presented as the mean ± SD, $n = 3$ individual experiments. **d** Schematic showing the composition of the preliminary cMSC and its working mechanism in MYC^{low} and MYC^{high} cells. The preliminary cMSC consisted of two parts. The first part was P_{aMYC}, which expresses the GOI expression cassette whose 3′-UTR contains ten sequences of split-ribozyme-1 (split-1) in tandem. The second part consisted of P_{rMYC} expressing split-ribozyme-2 (split-2). The working mechanisms of the preliminary cMSC in cells are as follows: In MYC^{low} cells (left), low expression of c-MYC results in low activity of P_{aMYC} and high activity of P_{rMYC}. In step 1, P_{aMYC} resulted in weak mRNA (GFP-10×split-1) transcription, whereas P_{rMYC} exhibited strong transcription of split-2. In step 2, a large amount of split-2 would interact with GFP-split-1, leading to the degradation of GFP mRNA through the ribozyme-based mRNA degradation process, resulting in almost no expression of GFP (step 3). In MYC^{high} cells (right), high expression of c-MYC resulted in high activity of P_{aMYC} and low activity of P_{rMYC}. P_{aMYC} resulted in strong mRNA (GFP-10×split-1) transcription, whereas P_{rMYC} resulted in weak transcription of split-2. In step 2, a small amount of split-2 would partly interact with GFP-split-1, leading to only partial degradation of the GFP mRNA, which led to a small amount of GFP translation (step 3). **e** Schematic showing the composition of the optimized cMSC and its working mechanism in MYC^{low} and MYC^{high} cells. The optimized cMSC consists of two parts. First, 6 binding sites of KLFa (6×KLFa-BS) were inserted upstream of P_{aMYC}. The reengineered P_{aMYC} (containing KLFa-BS) was used to drive the expression of a 5′ cassette encoding GFP, a T2A coding sequence, a cassette encoding KLFa and 3′ split-ribozyme-1 in tandem (GFP-T2A-KLFa-10×split-1). In the other part, P_{rMYC} was used to express split-ribozyme-2 (split-2). The working mechanisms of the optimized cMSC in cells are as follows: In MYC^{low} cells (left), low expression of c-MYC results in low activity of P_{aMYC} and high activity of P_{rMYC}. In step 1, P_{aMYC} resulted in weak mRNA (GFP-T2A-KLFa-10×split-1) transcription, whereas P_{rMYC} exhibited strong transcription of split-2. In step 2, a large amount of split-2 would interact with the mRNA of GFP-T2A-KLFa-10×split-1, leading to the degradation of GFP-T2A-KLFa-10×split-1 mRNA through the ribozyme-based mRNA degradation process, resulting in almost no expression of GFP (step 3). In MYC^{high} cells, high expression of c-MYC resulted in high activity of P_{aMYC} and low activity of P_{rMYC}. In step 1, a large amount of GFP-T2A-KLFa-10×split-1 is transcribed by P_{aMYC}, whereas a small amount of split-2 is produced by P_{rMYC}. In step 2, some GFP-T2A-KLFa-10×split-1 mRNAs interacted with split-2 and were degraded, whereas others were retained for the next step of translation. In step 3, small amounts of GFP and KLFa were translated. In step 4, the successfully translated KLFa is transferred to the nucleus, where it binds to the KLFa-BS upstream of P_{aMYC}, reactivating it (step 5) to transcribe more GFP-T2A-KLFa-10×split-1 mRNA (step 6) and translation (step 7). This positive feedback loop would generate an increasing amount of GFP-T2A-KLFa-10×split-1 mRNAs so that the degradation effect of split-2 transcribed by P_{rMYC} on GFP-T2A-KLFa-10×split-1 mRNA was negligible in this scenario. **f** Determining the mean fluorescence intensity (MFI) of GFP-driven expression by the preliminary cMSC and the optimized cMSC in BFP^+ cells over a range of siRNA and tetracycline concentrations. The data were presented as the mean ± SD, $n = 3$ individual experiments.

resulted in almost no GFP expression (0.21%), indicating that the preliminary cMSC caused almost no background expression of MYC^{low}. However, in MYC^{high}, the efficiency of the preliminary cMSC (that is, the ratio of GFP^+/BFP^+ cells) was 17.9% (Fig. 2f and Supplementary Fig. 3d–f), which was lower than that of P_{aMYC}-GFP (43.4%). The utilization of P_{rMYC}-mediated ribozyme-based translational inhibition can eliminate unwanted background expression of P_{aMYC} in MYC^{low}, but it decreases the efficiency of P_{aMYC} in MYC^{high}.

To improve the efficiency of the preliminary cMSC in MYC^{high}, we designed a feedforward loop amplifying GOI expression based on a transcriptional activator[31]. A synthetic transcriptional activator (KLFa) generated by fusing the viral VP64 transcriptional activation domain with the zinc finger-based transcriptional activator KLF6 was used in the optimization of the preliminary cMSC. We reprogrammed the DNA-binding domain of KLF6 in KLFa to avoid crosstalk between KLFa and other endogenous components[36]. Next, multiple KLFa binding sites (KLFa-BS) were encoded in the 5′ P_{aMYC}, which drove the expression of a 5′ cassette encoding GOI (GFP), a T2A coding sequence, a cassette encoding KLFa and the 3′ split-ribozyme-2 in tandem (Fig. 2e). In addition, P_{CMV}-BFP was inserted upstream of the optimized cMSC-GFP region and used to label the transfected cells. With respect to MYC^{low}, transfection of the optimized cMSC-GFP resulted in almost no GFP expression (0.12% and 0.45%, respectively), indicating excellent inhibition of the optimized cMSC in MYC^{low} (Fig. 2f and Supplementary Fig. 3g–i). Notably, the efficiency of the optimized cMSC reached 86.0% in MYC^{high} (5.5-fold greater than that of the preliminary cMSC), which indicated that the cMSC optimized by the KLFa-feedforward loop exhibited robust improvement in efficiency in MYC^{high}.

The design of the ribozyme-based target mRNA decay greatly reduced the probability of false-positive expression, which resulted in almost no activation of GOI expression driven by the cMSC in MYC^{low}. Moreover, the ability of KLFa-based feedforward loops to amplify GOI expression allowed the cMSC to have robust activation efficiency in MYC^{high}. Taken together, this design generated a high output only in MYC^{high}, demonstrating the stringency and therapeutic safety of our circuit architecture.

Characterization of the ability of a cMSC to distinguish physiological and pathological c-MYC expression

To characterize the ability of a cMSC to distinguish pathological c-MYC expression, we first detected the expression profile of c-MYC in bladder cancer. We quantified c-MYC expression based on the mRNA transcription levels of c-MYC, which were normalized to those of GAPDH. We found that, compared with normal associated tissue (NAT), bladder cancer tissue presented high c-MYC expression (Supplementary Fig. 5a). We established a mathematical model that describes the working properties of the cMSC platform. This mathematical model predicted that the cMSC would begin to activate the output of GOI expression when the endogenous c-MYC mRNA expression level reached ~2.8 times the GAPDH expression level, whereas the activation of the cMSC would reach saturation when the endogenous c-MYC mRNA expression reached ~32.4 of the GAPDH expression level.

We further determined the efficiency of the optimized cMSC in primary cells. Compared with normal cells, U2OS, T24, and UMUC3 cells transfected with cMSC-GFP presented greater expression of GFP than did normal iPSCs and COS-7, C2C12, RWPE-1 and SVHUC1 cells (Supplementary Fig. 5b, c). Next, we investigated the further application of the cMSC in vivo, and its efficiency was determined in human xenograft tumor mouse models and patient-derived organoids using an adeno-associated virus (AAV). GFP was used for GOI-driven expression by the cMSC. We used U2OS and T24 cells, which express low and high levels of endogenous c-MYC, respectively, to establish mouse models of human xenograft tumors (Supplementary Fig. 5d). Notably, after AAV-mediated cMSC transfection, tumor tissue derived from T24 cells presented 12.6-fold greater GFP activation than did that derived from U2OS cells, indicating that the cMSC can sense different levels of endogenous c-MYC expression in tumor tissues and drive the expression of GOI at different levels accordingly (Supplementary Fig. 5e, f). To further demonstrate the value of the cMSC for clinical application and clinical transformation, we investigated the efficiency of the cMSC in human organoids. Three organoids were used to evaluate the efficiency of the cMSC, including one normal organoid (organoid-N) derived from bladder mucosal epithelial cells and two bladder cancer organoids derived from bladder cancer patients in the early stage (organoid-BC1) and advanced stage (organoid-BC2). The expression levels of endogenous c-MYC in the organoids were quantified via qPCR (Supplementary Fig. 5g). As expected, the cMSC presented relatively greater GFP expression in organoid-BC2 (4.2-fold) with high endogenous c-MYC expression than in organoid-BC1, and importantly, the cMSC presented almost no GFP-driven expression in organoid-N (Supplementary Fig. 5h, i).

Design and validation of the cell-to-cell system

To overcome ITH and improve the efficiency of cancer therapy, we proposed and characterized the CtC system based on directed programmed cell–cell communication. The CtC system employs a two-step process: (1) the described gene circuit transfects the first susceptible cells (e.g., tumor cells with MYC^{high}) and (2) the mRNA of the gene circuit is shuttled from the first transfected cells to the second surrounding nonsusceptible cells (e.g., tumor cells with MYC^{low}) via CtC events (Supplementary Fig. 6a). For this purpose, we developed a CtC system to produce truncated CRISPR-dCas13d-based exosomes, which can carry target mRNAs of interest (ROIs) and directly deliver them from cancer cells with MYC^{high} to target cells with MYC^{low}. In detail, the truncated dCas13d (trCas13d) was fused to the C-terminus of CD63 (P_{CMV}-CD63-trdCas13d), a marker membrane protein of the exosome, and the direct repeat (DR) of the crRNA was inserted into the 3′-untranslated region (3′-UTR) of the reporter GOIs (Supplementary Fig. 6b–e). The ROIs encoding the reporter GOIs could be well incorporated into exosomes via the interaction between trCas13d and the DR structure in the 3′-UTR of the ROIs.

We systematically validated various aspects of the CtC-based mechanism. We first examined whether CRISPR-dCas13d-based engineered exosomes effectively package ROIs. For this purpose, we performed a series of proof-of-principle assays and tested them. We used an expression vector (PGK-GFP) to express the GFP gene and inserted a DR structure in the 3′-UTR (PGK-GFP^{DR}) as the reporter GOI (Supplementary Fig. 6f, g). Compared with those in the other control groups, we observed significant enrichment of GFP mRNA in the exosomes isolated from the supernatant of 293 T cells cotransfected with P_{CMV}-CD63-trCas13d and PGK-GFP^{DR} (Supplementary Fig. 6f, g). As expected, after coculturing exosomes derived from 293T cells (cotransfected with P_{CMV}-CD63-trCas13d and PGK-GFP^{DR}) with T24 cells, we detected significant expression of GFP, whereas almost no GFP expression was detected in the control group of cells (Supplementary Fig. 6f, g). In addition, engineered exosomes labeled with FITC (anti-His-tag/FITC) accumulated in T24 cells over time (Supplementary Fig. 6h).

Next, we characterized whether engineered exosomes equipped with a target module could be endocytosed more efficiently into target cells. First, we analyzed the expression characteristics of tumor-related membrane proteins based on the c-MYC expression profile in bladder cancer cells. We found that, compared with NATs, bladder cancer tissues presented high expression of mucin-1 (MUC1) (Supplementary Fig. 6i). Interestingly, in the single-cell sequence, we found that in bladder cancer cells, MYC^{low} cells presented increased MUC1 expression (Supplementary Fig. 6j–l). Based on these features, we introduced a target module by conjugating the MUC1 scFv to the N-terminus of Lamp2b (P_{CMV}-MUC1 scFv-Lamp2B) to mediate the ability of engineered exosomes to target MYC^{low} cancer cells. Lamp2b, a lysosome-

associated membrane protein, is widely expressed in exosome membranes[37]. The targeted modification of exosomes can be achieved by genetically fusing targeting peptides or specific ligands to the N-terminus of Lamp2b[38].

The expression level of MUC1 in T24 cells was much greater than that in SVHUC1 cells; thus, these two cell lines were selected for further determination (Supplementary Fig. 6m). The engineered exosomes, which were equipped with targeting modules and extracted from the cell supernatants of 293T cells cotransfected with P_{CMV}-CD63-trCas13d, P_{CMV}-MUC1 scFv-Lamp2b and PGK-GFP^{DR}, were cocultured with T24 or SVHUC1 cells (Supplementary Fig. 6n, o). We found that the expression of GFP in T24 cells was significantly greater than that in SVHUC1 cells, indicating that the targeting modules enhance the efficiency of exosome delivery of the ROIs to target cells (Supplementary Fig. 6p). To further substantiate this result, we cocultured engineered exosomes equipped with targeting modules with T24 cells that had been transfected with different concentrations of siRNA for MUC1 and detected their GFP expression levels. We observed that the expression level of GFP decreased as the expression level of MUC1 in the cells decreased (Supplementary Fig. 6q). As demonstrated, we constructed CRISPR-based engineered exosomes that can deliver ROIs into cells for translation.

Applications of the cell-to-cell system

To determine the efficiency of the CtC system in cellular gene therapy, we designed a proof-of-principle version of the CtC system and validated it in 293T cells. To this end, we established stably transfected 293T cells that stably overexpress c-MYC and MUC1 and then cocultured them at a 1:1 ratio. We constructed an expression vector (cMSC-GFP^{DR}) using a cMSC to express GFP^{DR} to validate whether the mRNAs of GFP shuttle from MYC^{high} cells to MYC^{low} cells through the CtC communication pathway. To characterize the CtC system efficiency more quantitatively, we inserted an mCherry expression cassette driven by a cMSC upstream of cMSC-GFP^{DR} in cMSC-GFP^{DR} to label the transfected cells (Fig. 3a). We subsequently constructed an expression vector (cMSC-CtC) to express the engineered exosome, which consisted of a CD63-trdCas13d expression cassette, a T2A coding sequence, and a 3′ cassette encoding MUC1 scFv-Lamp2B for carrying GFP mRNA as described above (Fig. 3a). As expected, transfection of cMSC-GFP^{DR} resulted in all GFP and mCherry being coexpressed in the same MYC^{high} cells (Fig. 3b). Notably, when the cells were cotransfected with cMSC-GFP^{DR} and cMSC-CtC, there were GFP-expressing cells independent of those expressing both GFP and mCherry, indicating that GFP mRNAs were delivered from MYC^{high} cells to MYC^{low} cells via the CtC pathway (Fig. 3b). We then quantified the ratio of GFP-positive cells to mCherry-positive cells via flow cytometry and found that the ratio of GFP$^+$ cells was ~1.4-fold greater than that of mCherry$^+$ cells via CtC events (Fig. 3c, d). Notably, there was no significant difference in the total expression of GFP between the two groups (Fig. 3e). These results indicated that in the CtC events, the total expression of the GOI in the whole-cell population was invariable, but the number of GOI-expressing cells increased because of the increase in exosome-based cell–cell communication. In other words, the CtC system would distribute the total GOI expression of the cell population to a larger number of cells.

We further investigated CtC events using AAV vectors in human xenograft tumor mouse models and a human bladder cancer organoid model. The AAV vector (AAV-CtC) expressing CtC components consisted of cMSC-CD63-trdCas13d-T2A-MUC1 scFv-Lamp2B. The AAV vector (AAV-GFP^{DR}) encoding the GFP gene driven by the cMSC and the labeled mCherry gene driven by the cMSC (cMSC-mCherry-cMSC-GFP^{DR}) were subsequently used to determine the CtC events in vivo. As expected, tumor tissues infected with AAV-GFP^{DR} expressed both GFP and mCherry, whereas tumor tissues infected with AAV-GFP^{DR} and AAV-CtC presented a large number of cells expressing GFP but not mCherry, which indicated that in the course of CtC events, many uninfected cells received and translated the mRNA of GFP carried by engineered exosomes (Fig. 3f, g). We also found that, in the organoids coinfected with AAV-GFP^{DR} and AAV-CtC, a certain proportion of the cells expressed only GFP but not mCherry because of CtC events (Fig. 3h, i). Together, CRISPR-based engineered exosomes could carry ROIs into surrounding cells and express them, which might overcome ITH through directed reprogramming of cell–cell communication.

The cMSC/CtC platform improves the efficiency of combinations of immunostimulatory factors triggering T cells to kill cancer cells specifically

We sought to encode immunotherapy as an output of the cMSC/CtC platform and validate its therapeutic efficacy. A surface T-cell engager (STE) was constructed by fusing a bispecific anti-CD3/CD28 single-chain variable fragment (scFv) with a human inert membrane anchor, and it was highly expressed in the cell membrane in vitro (Supplementary Fig. 7a–c). T-cell-mediated killing was clearly observed in the cMSC-STE-transfected tumor cells (Supplementary Fig. 7d, h). As expected, the cells expressing STE targeting both CD3 and CD28 exhibited greater T-cell-mediated killing efficiency and activation of both IFN-γ, TNF-α and interleukin-2 (IL-2) than those expressing STE targeting CD3[39,40] (Supplementary Figs. 6e–g, 7i–j). We hypothesized that a greater number of cells surface-expressing STE could induce stronger T-cell-mediated immunotherapy (Fig. 4a). To substantiate this hypothesis, we used the CtC system to carry STE mRNA for diffusion into surrounding tumor cells and translation. We found that the CtC system could mediate the expression of STE in more tumor cells and increase T-cell-based tumor immune killing efficiency (Fig. 4b–f).

Because combination therapy has a more efficient therapeutic effect than monotherapy[41], we designed cMSC-mediated outputs of multiple immune modulators to optimize these cancer-specific gene circuits (Fig. 4g). We used a cytokine that enhances T-cell activation (IL-21) and function, an immune checkpoint inhibitor (anti-PD1) and a chemokine that promotes T-cell transport to the tumor site (CCL5), in combination with STE for immunotherapy. Interleukin (IL)−21 is an important immunostimulatory cytokine that has shown adjuvant antitumor activity in several preclinical models[42]. In addition, high c-MYC expression initiates insensitivity to immunotherapy and mediates immune evasion through the modulation of the PD1/PDL1 pathway[25,26,43]. Chemokines are critical for T-cell accumulation in solid tumors, and CCL5 overexpression is associated with T-cell infiltration in solid tumors[44].

Next, we validated the efficiency of cMSC/CtC-mediated cancer immunotherapy in an in vivo model of human bladder cancer. We constructed AAV vectors encoding cMSC packages expressing STE^{DR}, IL-21, anti-PD1 and CCL5 (cMSC^{SIPC}). In addition, we constructed another AAV for delivering the designed CtC system for delivering the mRNA of STE specifically (CtC^S) (Fig. 4g). We established humanized mouse models and intratumorally injected AAVs into mouse tumors, followed by monitoring the tumor volume to Day 30 (Fig. 4h). Compared with those of the AAV^{mock} group, the cancer immunotherapy efficiencies of the cMSC, cMSC^{SIPC} and cMSC^{SIPC}/CtC^S groups were significantly reduced by 65%, 86% and 99.2%, respectively. Notably, the group infected with AAV^{SIPC}/CtC^S presented the most efficient tumor suppression, the longest survival time and the highest level of IFN-γ (Fig. 4i–l). All the AAV treatments had no effect on the weight of the mice (Fig. 4m). Furthermore, the AAV^{SIPC}/CtC^S group presented the lowest expression of the proliferation marker Ki67 and the highest expression of the apoptosis marker TUNEL (Supplementary Fig. 7h–k). Therefore, through comprehensive analysis of the above data, we found that the cMSC/CtC-mediated combination of immunostimulatory factors could trigger robust T-cell-mediated tumor killing.

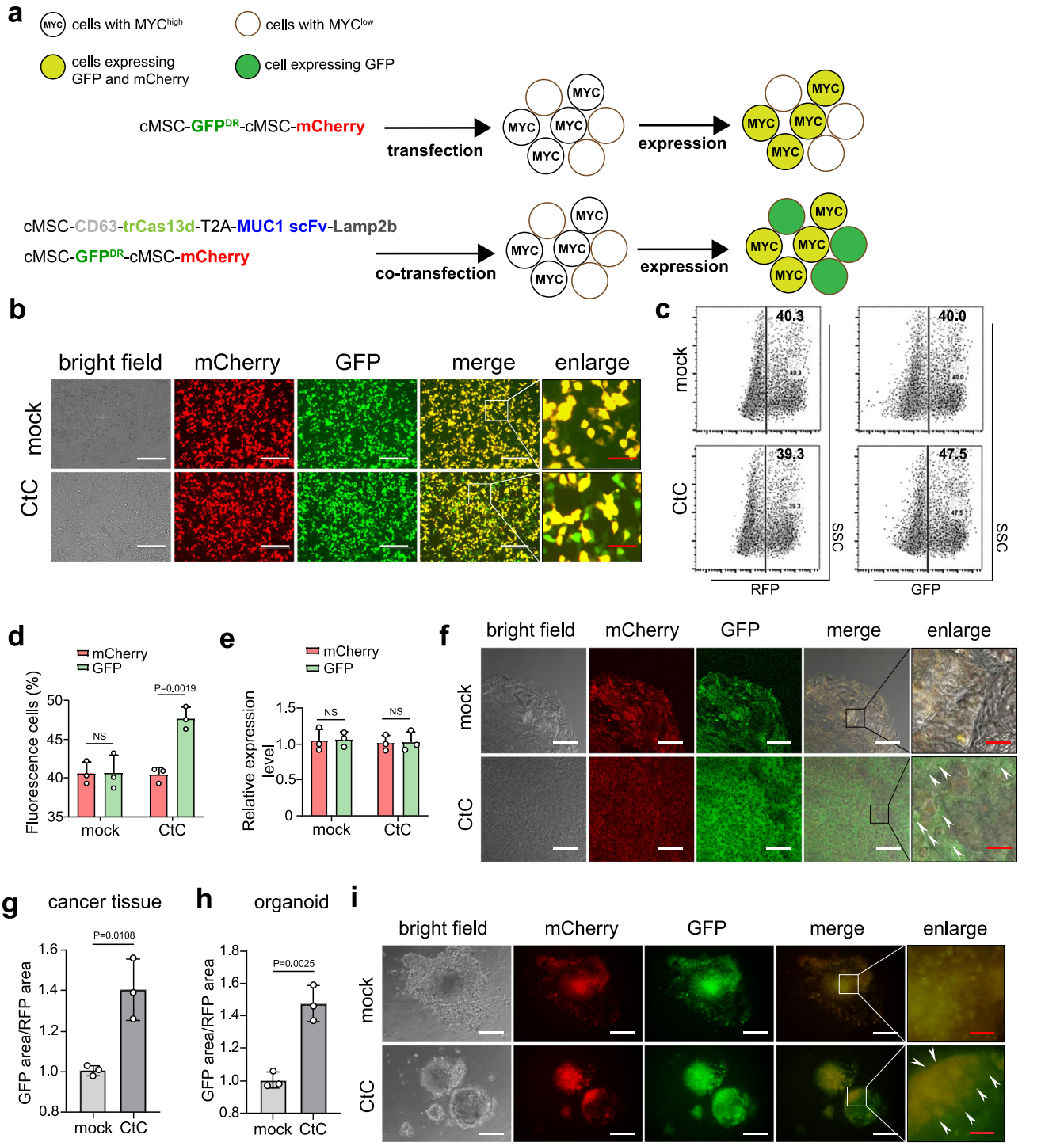

cMSC^{SIPC}/CtC^{S} triggers potent T-cell-mediated tumor-specific killing without the limitations of ITH

Next, we determined the efficiency by which the cMSC/CtC platform can trigger specific T-cell-mediated cancer immunotherapy to overcome the limitations of ITH. The bladder cancer cell line RT4, which is derived from early-stage bladder cancer tissue, has a very low basal expression level of c-MYC. To simulate MYC^{low} tumor cells, we stably expressed CMV-mCherry in RT4 cells, whereas to simulate MYC^{high} tumor cells, we stably expressed CMV-MYC-T2A-GFP in the same cell line. These two types of cells were then mixed and cocultured at a 1:1 ratio to simulate a tumor model with heterogeneous c-MYC expression. In an in vitro assay, coculture of cMSC^{SIPC}-transfected cells (RT4-mCherry/RT4-GFP) with PBMCs resulted in a significant T-cell-mediated killing effect of RT4-GFP (98%) compared with RT4-mCherry (17.8%) (Fig. 5a–c). Notably, when cMSC^{SIPC}/CtC^{S}-transfected cells were cocultured with peripheral blood mononuclear cells (PBMCs), both RT4-mCherry (96%) and RT4-GFP (100%) exhibited significant T-cell-mediated killing effects (Fig. 5a–c). Furthermore, cMSC^{SIPC}/CtC^{S} mediated a stronger immunotherapy response than did cMSC^{SIPC} in the RT4-mCherry/RT4-GFP cell populations (Fig. 5d–f). Hence, the cMSC/CtC platform has promising therapeutic potential for overcoming ITH.

In vivo, we generated a mixture of RT4-mCherry and RT4-GFP xenograft tumors in NSG mice and performed human immune rebuilding followed by intratumoral injection of different AAV systems, PBS, or anti-PD1 therapy (Fig. 5g). Here, anti-PD1 therapy

Fig. 3 | Design and characterization of the CtC platform. a Schematic showing the proof-of-principle assay of the CtC platform. Two expression vectors were used here. First, there were two independent cMSC systems expressing GFP^{DR} (cMSC-GFP^{DR}) and mCherry (cMSC-mCherry). The cMSC-GFP^{DR} and cMSC-mCherry strains were constructed with the same expression vector (Reporter vector). Second, a cMSC was used to drive the expression of the 5′ CD63-trCas13d expression cassette and the T2A and 3′ MUC1 scFv-Lamp2b expression cassettes (CtC expression vector). In the cells transfected with the reporter vector, both GFP and mCherry were expressed in the MYC^{high} cells simultaneously. In the cells cotransfected with the reporter vector and the CtC expression vector, GFP was expressed in the MYC^{high} cells, and its mRNA could be packaged into the CtC exosomes for shuttling to nearby cells, especially those with high MUC1 expression. mCherry was expressed in only the MYC^{high} cells, which were used to label the transfected cells. **b**–**d** Representative images (**b**) of cells transfected with the reporter vector alone (mock group, top) and cotransfected with the reporter vector and the CtC expression vector (CtC group, bottom) are shown. FACS analysis of GFP and mCherry expression (**c**). FACS was used to quantify the proportion of GFP-positive and mCherry-positive cells among the 293T cells transfected as described above (**d**). These data indicated that the presence of CtC events resulted in more cells in the group expressing GFP. The data were presented above as the mean ± SD, $n = 3$ individual experiments, and significance was determined via two-tailed Student's *t*-tests, NS not significant. Scale bar: 300 μm (the line in white) and 50 μm (the line in red). **e** Quantification of the expression levels of GFP and mCherry in a qPCR assay. These data indicated that the presence of CtC events could not increase the total amount of GFP expressed in a cell population. The data were presented above as the mean ± SD, $n = 3$ individual experiments, and significance was determined via two-tailed Student's *t*-tests; NS not significant. **f**, **g** Illustration of CtC events in a cancer xenograft model. GFP and mCherry expression in T24 tumor tissue infected with AAV (cMSC-GFP^{DR}-cMSC-mCherry) alone or with both AAV (cMSC-CD63-dCas13d) and AAV (MSC-GFP^{DR}-cMSC-mCherry) (**f**). Areas marked by white arrows represent spatial segregation of GFP and mCherry fluorescence, indicating non-overlapping cellular expression domains. FACS quantification confirmed the differential distribution of GFP-positive versus RFP-positive cells (**g**). The data were presented above as the mean ± SD, $n = 3$ individual experiments, and significance was determined via two-tailed Student's *t*-tests. Scale bar: 300 μm (the line in white) and 50 μm (the line in red). **h**, **i** Illustration of CtC events in bladder cancer organoids. Quantification of GFP-positive and mCherry-positive cells in bladder cancer organoids (**h**). The tissue indicated by the white arrow is the tissue where GFP and mCherry expression are not colocalized. Bladder cancer organoids were infected with the above treatments (**i**). The data were presented above as the mean ± SD, $n = 3$ individual experiments, and significance was determined via two-tailed Student's *t*-tests. Scale bar: 300 μm (the line in white) and 50 μm (the line in red).

exhibited mild tumor-suppressive effects (Fig. 5h and Supplementary Fig. 8a). Notably, $cMSC^{SIPC-}$ and $cMSC^{SIPC}/CtC^{S}$-mediated immunotherapy showed robust tumor-suppressive effects, and the most remarkable tumor clearance efficiency was observed in the $cMSC^{SIPC}/CtC^{S}$ group (Fig. 5h and Supplementary Fig. 8a). Compared with those in the other groups, the mice treated with $cMSC^{SIPC}/CtC^{S}$ exhibited greater activation of IFN-γ-, TNF-α- and IL-2-producing $CD4^{+}$ and $CD8^{+}$ T cells (Fig. 5j–o). Next, we harvested tumor tissues from each group and analyzed the proportions of cells with high and low c-MYC expression. Interestingly, the surviving cells in the tumor tissues of the $cMSC^{SIPC}$ group had low c-MYC expression, whereas tumor cells with both high and low c-MYC expression were killed in the $cMSC^{SIPC}/CtC^{S}$ group (Supplementary Fig. 8b). Together, these data indicate that CtC-mediated mRNAs of STE are shuttled between tumor cells with high and low c-MYC expression, thereby effectively overcoming the limitations of ITH and improving tumor eradication efficiency.

To further clarify the tumor therapeutic effect of the cMSC/CtC platform on ITH, we validated the results in patient-derived tumor xenograft (PDX) mice followed by human immune rebuilding (Fig. 5p). As expected, the $cMSC^{SIPC}/CtC^{S}$ group showed significantly better therapeutic effects than the other groups did, such as the AAV-blank, anti-PD1 and $cMSC^{SIPC}$ groups (Fig. 5q, r and Supplementary Fig. 8j). Consistently, the mice treated with $cMSC^{SIPC}/CtC^{S}$ presented the highest activation of IFN-γ-, TNF-α- and IL-2-producing CD4+ and CD8 + T cells (Supplementary Fig. 8c–i). In addition, almost all the remaining tumor cells after $cMSC^{SIPC}$-mediated PDX treatment presented low c-MYC expression, indicating that $cMSC^{SIPC}$ could not effectively eliminate tumor cells with low c-MYC expression, which resulted in a lower therapeutic effect of $cMSC^{SIPC}$ than of $cMSC^{SIPC}/CtC^{S}$ (Supplementary Fig. 8k). Overall, the AAV-mediated cMSC/CtC platform could trigger robust and specific T-cell immunotherapy without the limitations of ITH.

Therapeutic efficacy of cMSC/CtC-based cancer immunotherapy in a humanized orthotopic bladder cancer model

The therapeutic efficacy of $cMSC^{SIPC}/CtC^{S}$ was first determined in humanized orthotopic murine models of bladder cancer via intravesical instillation. We performed four controlled assays, including an evaluation of the therapeutic efficiency of a blank AAV suspension, two types of traditional drugs used for intravesical instillation of bladder cancer (Bacillus Calmette Guerin vaccine (BCG) and mitomycin C) and a combined chemotherapy regimen (gemcitabine and cisplatin) to determine the efficacy and specificity of $cMSC^{SIPC}/CtC^{S}$ (Fig. 6a, b). The tumor volumes in the intravesical instillation groups of blank AAV, BCG and mitomycin C were significantly larger than those in the $cMSC^{SIPC}/CtC^{S}$ group, in which tumors were undetectable in half of the mice (Fig. 6b–d). The combination of gemcitabine and cisplatin, while having a significant antitumor effect, was also observed to have noticeable toxicity in mice. Furthermore, the $cMSC^{SIPC}/CtC^{S}$ group also had prolonged survival (Fig. 6e). The weights of the mice in the blank AAV, BCG, mitomycin C, and $cMSC^{SIPC}/CtC^{S}$ groups were not significantly different, whereas those in the gemcitabine and cisplatin groups were markedly lower, indicating noticeable toxicity associated with the combination therapy (Fig. 6f). Consistent with the therapeutic effect, the IFN-γ, TNF-α and IL-2 levels were significantly greater in the $cMSC^{SIPC}/CtC^{S}$ group than in the other groups, suggesting a stronger effect of immunotherapy (Fig. 6g–i). In the blank AAV group, the tumors were so large that they occupied almost the entire bladder cavity in all five mice (Supplementary Fig. 9). In the BCG, mitomycin C and combination therapy groups, although the tumor volumes were smaller than those in the blank AAV group were, there were sublarge areas of necrosis or dysmorphic growth patterns in the bladder mucosal epithelium (Supplementary Fig. 9). Remarkably, the most significant tumor suppression was observed in the mice intravesically instilled with $cMSC^{SIPC}/CtC^{S}$, and the bladder mucosal epithelia in the mice remained almost intact and healthy (Supplementary Fig. 9). Taken together, these data indicate the enormous clinical potential of intravesical instillation therapy in bladder cancer with AAV-based therapy.

Discussion

ITH leads to the diversity of tumor cell subset genotypes, and the current treatment has difficulty covering all genotypes, which is the essence of tumor treatment failure and recurrence[45,46]. The development of a treatment covering tumor cells of different genotypes is challenging, and there is still no strategy for treating ITH. As a common driver of human cancers, pathologic c-MYC expression not only promotes the occurrence and progression of tumors but also accelerates the development of ITH. Based on the characteristics of c-MYC expression, tumor cells can be roughly divided into high- and low-expression subgroups to simplify the classification of high-ITH tumor cells. Here, we established a versatile c-MYC-based gene circuit platform. For tumor cells with high expression of c-MYC, the cMSC can identify and trigger selective T-cell-mediated killing of cancer cells, and cancer cells with low c-MYC expression can also receive corresponding

https://doi.org/10.1038/s41467-025-63377-3

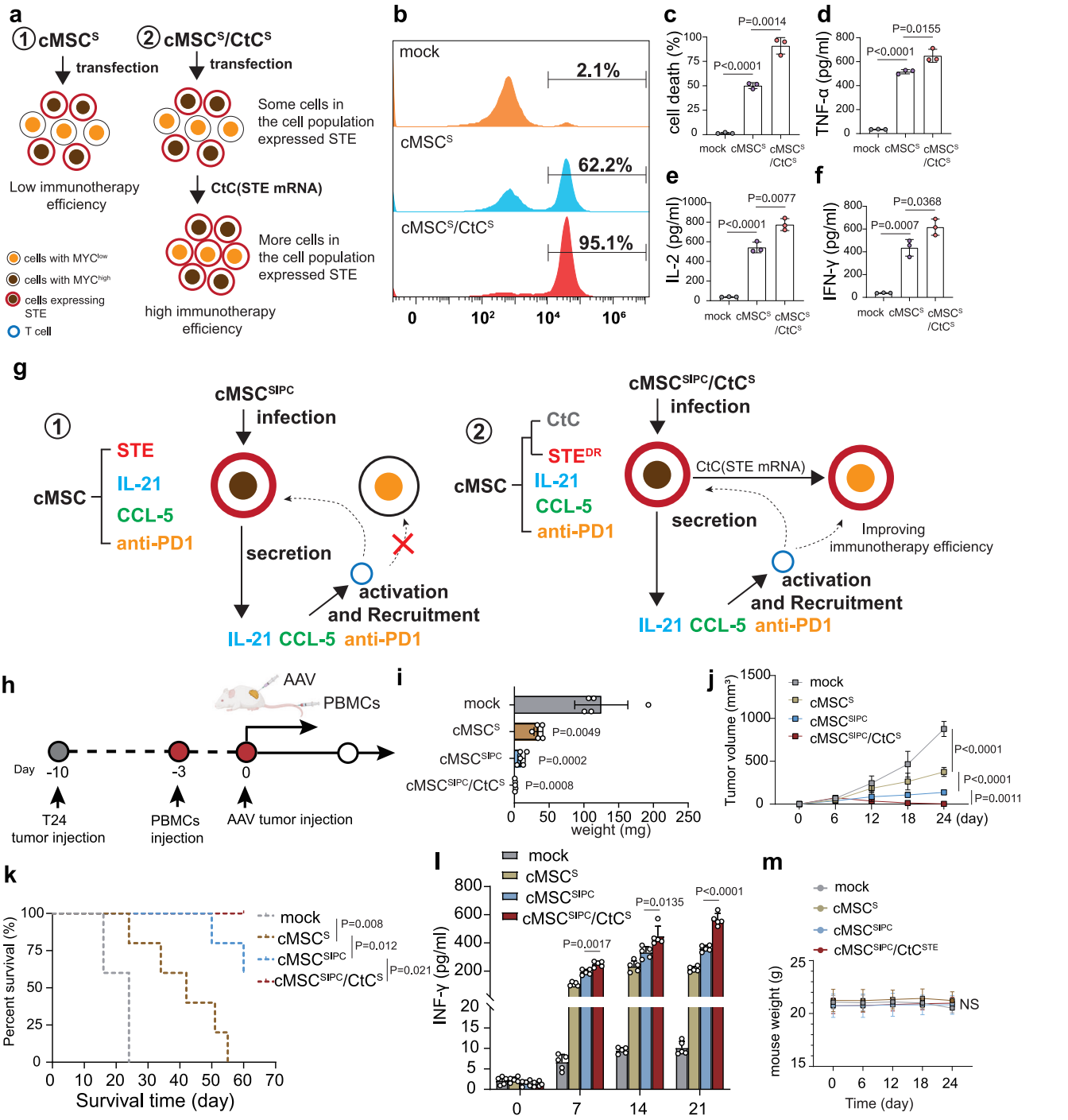

tumor immunotherapy through the CtC system to eliminate the ineffective tumor treatment caused by ITH.

Although many exciting studies have focused on targeting c-MYC for cancer therapy, it is difficult to avoid interference with normal cells. Directly targeting the degradation or inhibition of MYC function through effective synthetic elements can effectively kill tumors, but these strategies indiscriminately interfere with c-MYC activity in normal cells[17,18]. To address this, we detected the expression of c-MYC in normal and cancer tissues and developed a c-MYC-based gene circuit platform based on the bidirectional interaction between P_{aMYC} and P_{rMYC}. Mechanistically, P_{aMYC} is activated by c-MYC/MAX dimers via different expression gradients of c-MYC, which is manifested as a positive correlation between the activity of PaMYC and the expression level of c-MYC. P_{rMYC} is negatively regulated by different c-MYC expression gradients through the inhibition of MIZ-1-mediated promoter activation. The activation threshold of cMSC is determined by P_{aMYC}, P_{rMYC}, and the ribozyme switch. In the construction of cMSC, P_{rMYC} is used to trigger the ribozyme switch to counteract the unwanted background expression of P_{aMYC}, ensuring that the entire cMSC system is activated only above a certain c-MYC threshold. In our study, only the endogenous c-MYC mRNA expression level reached 2.7519 of the GAPDH expression level, which can activate the cMSC to express GOIs. This c-MYC-dependent activation threshold of the cMSC is applicable to a variety of tumor types, such as bladder and prostate cancers. Other distinct tissues and cell types may support varying levels of c-MYC expression, and different application scenarios demand different cMSC activation thresholds. Nevertheless, based on the modular design of P_{aMYC}, P_{rMYC}, and ribozyme-switch, the c-MYC-

Fig. 4 | Improving the efficiency of cancer immunotherapy via the cMSC/CtC platform. a Schematic showing cMSC/CtC-mediated STE diffusion in cell populations to improve the efficiency of cancer immunotherapy. In panel 1, CtC events were not detected. In a tumor population, only some cancer cells expressed STE because of ITH or incomplete transfection efficiency, which resulted in low immunotherapy efficiency. In panel 2, CtC events were present. cMSC/CtC-mediated STE diffusion in cell populations increases the number of STE-expressing cancer cells, which results in improved efficiency of cancer immunotherapy. **b** Mock group: T24 cells transfected with the cMSC vector expressing a nonfunctional polypeptide; cMSC group: T24 cells transfected with the cMSC vectors expressing STE for targeting CD3 and CD28 (cMSC-STE^{DR}); cMSC/CtC^{S} group: T24 cells cotransfected with cMSC vectors expressing STE for targeting CD3 and CD28 (cMSC-STE^{DR}) and a cMSC vector expressing the CtC expression component (cMSC-CD63-trCas13d-T2A-MUC1 scFv-Lamp2b). To characterize STE display and expression levels on cell surfaces, the transfected T24 cells were stained with phycoerythrin-labeled anti-His tag Ab/PE. The proportion of STE-expressing cells in each group was evaluated by flow cytometry. **c** Proportions of dead T24 cells in the mock, cMSC and cMSC/CtC^{S} groups; $n = 3$ individual experiments. The data were presented above as the mean ± SD, and significance was determined via two-tailed Student's *t*-tests. **d**–**f** The expression levels of TNF-α (**d**), IL-2 (**e**), and IFN-γ (**f**) in the medium after incubation with PBMCs from T24 cells in the mock, cMSC and cMSC/CtC^{S} groups, respectively, $n = 3$ individual experiments. The data were presented above as the mean ± SD, and significance was determined via two-tailed Student's *t*-tests. **g** CtC-mediated STE diffusion can further improve the efficiency of immunotherapy induced by a combination of immunostimulatory factors. In panel 1, CtC events were not detected. In a tumor population, only some cancer cells expressed STE because of ITH or incomplete transfection efficiency, which resulted in low immunotherapy efficiency in non-STE-expressing cancer cells. In panel 2, CtC events were present. cMSC/CtC-mediated STE diffusion in cell populations increases the number of STE-expressing cancer cells, which results in high-efficiency cancer immunotherapy. **h** Schematic illustration of the treatment schedule in the mouse model of T24 bladder cancer cells. Created in BioRender. Zhan, H. (2025) https://BioRender.com/ckseent. **i**, **j** Average tumor weight (**i**) and average tumor growth kinetics (**j**) of the mice subjected to different treatments: mock, cMSC, cMSC^{SIPC}, and cMSC/CtC^{S}. The tumor volume (mm^3) was monitored daily using a caliper. The data were presented as the mean ± SD ($n = 5$ mice), and significance was determined via two-tailed one-way ANOVA. **k** Kaplan–Meier survival curves of various groups. A log-rank (Mantel–Cox) test was performed to compare survival between groups ($n = 5$ mice per group). **l** The level of serum IFN-γ was determined by ELISA on Days 0, 7, 14, and 21. The data were presented as the mean ± SD ($n = 5$ mice), and significance was determined via two-tailed Student's *t*-tests. **m** Mouse body weight was monitored and recorded. The data were presented as the mean ± SD ($n = 5$ mice), and significance was determined via two-tailed one-way ANOVA; NS not significant.

dependent activation threshold of the cMSC can be fine-tuned to meet specific application requirements. The increasing popularity of gene circuits in cancer therapy is attributed to their precise control over cellular activities. In accordance with these principles, we introduced a ribozyme-based switch to link P_{aMYC} and P_{rMYC}, which ensures that the cMSC is activated exclusively by a specific threshold of c-MYC. We further incorporated KLFa-mediated positive feedback to increase the expression of therapeutic genes by the cMSC. These design elements ensure that the cMSC platform precisely and efficiently regulates the expression of therapeutic genes. Therefore, the cMSC described here can be used to distinguish pathological from physiological c-MYC expression and shows great potential for developing specific tumor treatment strategies with high safety.

The lack of specific cell-surface antigens and ITH are two important factors in the consideration of the efficacy of immunotherapy[47]. Here, we characterized the cMSC/CtC platform to address these questions to improve the efficiency of cancer immunotherapy. First, we used a cMSC system to express STE on the surface of MYC^{high} cancer cells, as well as immunostimulatory agents. This approach may address the ineffectiveness of immunotherapy due to the lack of specific cell-surface antigens. Second, we established a CtC system to promote and utilize engineered exosomes secreted by MYC^{high} cancer cells in situ to deliver STE mRNA effectively to surrounding tumor cells not expressing STE. The overall efficiency of immunotherapy could be improved by the expression of STE in all cancer cells. In theory, the cMSC/CtC-mediated immunotherapy model may be suitable for multiple tumor types and may be a potential strategy to improve specific cancer immunotherapies.

The use of AAVs to deliver selective cancer immunotherapy driven by a cMSC can trigger a robust antitumor response and improve the survival rate of mice. AAV, derived from nonpathogenic wild-type adeno-associated viruses, is considered one of the most promising gene transfer vectors because of its high safety, low immunogenicity, long expression time of transgenes in vivo, and wide range of host applications[48]. There are currently several AAV-mediated gene therapies in clinical use, such as inherited retinal dystrophy[49] and spinal muscular atrophy (SMA)[50]. Bladder cancer is a common malignant tumor with high heterogeneity and recurrence, yet curative treatments are still not available[51]. The bladder cavity communicates with the outside via the physiological urethra, and intravesical instillation of drugs is the most common clinical therapy for bladder cancer. Unlike other types of cancers, AAV-mediated gene circuits can be delivered to bladder cancer via intravesical instillation, which is a natural advantage in bladder cancer therapy. However, the commonly used agents for intravesical instillation, such as BCG and epirubicin, have severe disadvantages. For example, patients who receive intravesical instillation of BCG and epirubicin experience severe symptoms of bladder irritation. BCG and epirubicin have poor antitumor efficacy and nonspecific therapy, which results in poor efficacy of cancer therapy and increases the probability of tumor recurrence and resistance. Here, we developed an intravesical instillation of AAV-mediated cMSC^{SIPC}/CtC^{S} that resulted in effective bladder tumor clearance and prolonged survival in mice but did not cause obvious damage to the bladder mucosa. These data indicated that cMSC^{SIPC}/CtC^{S}-mediated intravesical instillation into the bladder exhibited robust antitumor therapeutic efficacy and specificity in a mouse orthotopic bladder cancer model, which confirmed its great potential for clinical application and transformation. Notably, we are conducting preclinical trials to evaluate the efficacy and safety of AAV-mediated cMSC^{SICP}/CtC^{S} via intravesical instillation for treating bladder cancer.

However, the cMSC/CtC platform may fail to function properly under some extreme circumstances. First, the cMSC is designed to perform cell reprogramming by sensing different levels of c-MYC expression. Therefore, this mechanism may be compromised by germline mutations in c-MYC, even though such mutations are extremely rare. Second, c-MYC positively regulates P_{aMYC}, and P_{rMYC} negatively regulates it through MAX and MIZ-1. Although the P_{aMYC}- and P_{rMYC}-mediated cMSCs are regulated primarily by different c-MYC expression gradients, the characteristics of cMSCs regulated by c-MYC may be affected in special types of cells or tissues where MAX or MIZ-1 expression is extremely low or absent. Third, the expression of therapeutic genes mediated by the cMSC/CtC platform is predominantly activated by tumor cell populations with high c-MYC expression. Therefore, a greater proportion of c-MYC-high tumor cell populations correlates with enhanced therapeutic efficacy mediated by the cMSC/CtC platform. Conversely, this implies that therapeutic efficacy may be diminished in tumor types characterized by low c-MYC expression. In the context of bladder cancer therapy, the cMSC/CtC gene circuit platform is expected to show enhanced efficacy for the basal/squamous (Ba/Sq) subtype, which is often associated with increased c-MYC expression, whereas it may fail to achieve the anticipated therapeutic outcomes in some luminal subtype bladder cancers with extremely low c-MYC expression. In addition, to further advance the therapeutic applications of the cMSC/CtC platform, several issues must be

https://doi.org/10.1038/s41467-025-63377-3

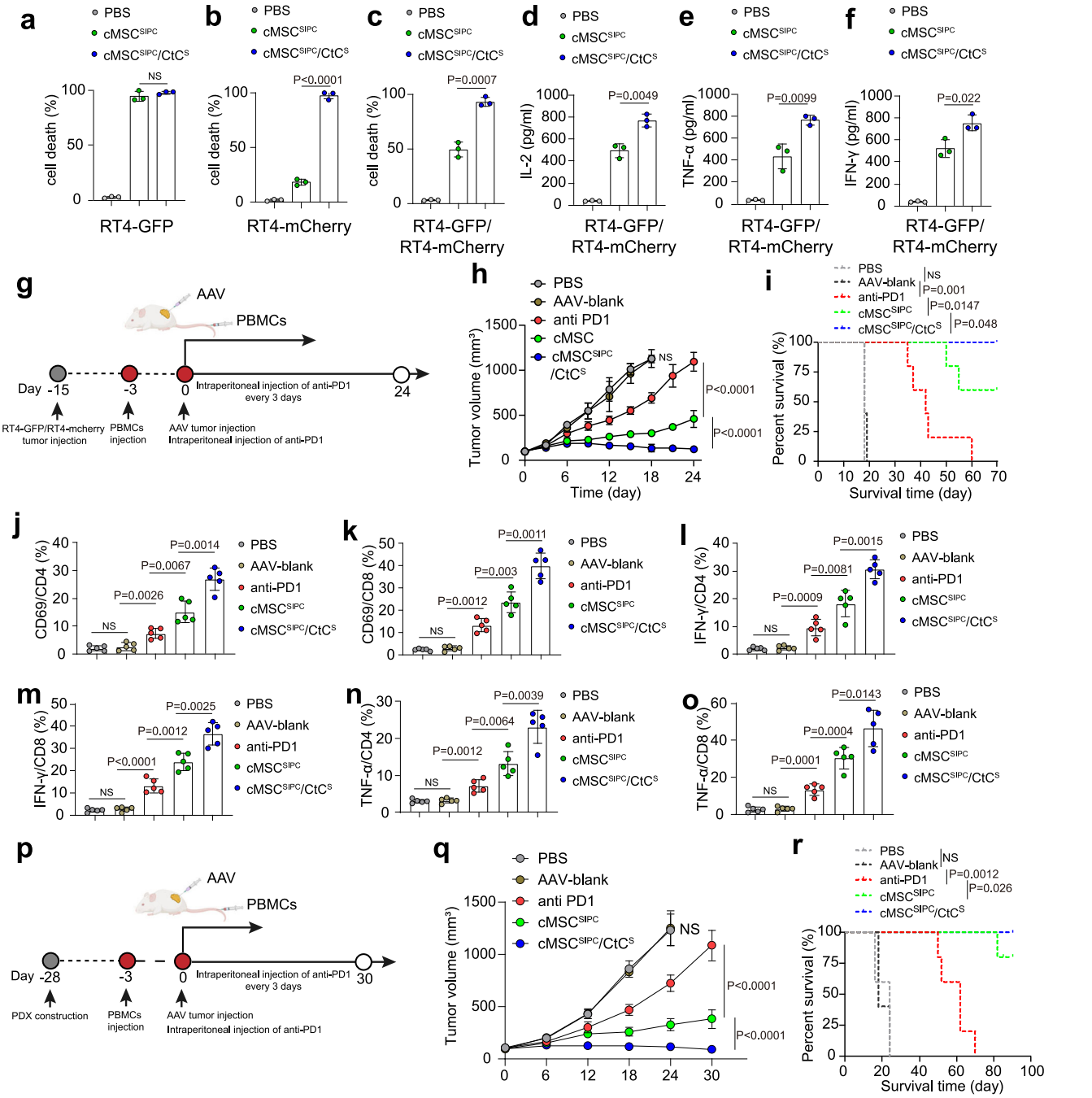

Fig. 5 | cMSC^{SIPC}/CtC^{S} triggers potent T-cell-mediated tumor-specific killing without the limitations of ITH. a–**c** Percentages of dead RT4-GFP (**a**), RT4-mCherry (**b**), and RT4-GFP/RT4-mCherry (**c**) cells treated with PBS, cMSC^{SIPC} or cMSC^{SIPC}/CtC^{S}, respectively. The data were presented as the mean ± SD; $n = 3$ individual experiments. Significance was determined via two-tailed Student's *t*-tests; NS not significant. **d**–**f** Total expression levels of TNF-α (**d**), IL-2 (**e**), and IFN-γ (**f**) in the supernatants of cells in the PBS, cMSC^{SIPC}, and cMSC^{SIPC}/CtC^{S} groups, respectively, $n = 3$ individual experiments. The data were presented as the mean ± SD, and significance was determined via two-tailed Student's *t*-tests. NS not significant. **g** Schematic illustration of the treatment schedule for the RT4-GFP/RT4-mCherry mouse model. Created in BioRender. Zhan, H. (2025) https://BioRender.com/ckseent. **h** Comparison of the tumor growth kinetics of RT4-GFP/RT4-mCherry mice subjected to different treatments: PBS, AAV-blank, anti-PD1, AAV (cMSC^{SIPC}), and AAV (cMSC^{SIPC}/CtC^{S}). The tumor volume (mm^3) was monitored daily using the caliper method. The data were presented as the mean ± SD ($n = 5$ mice), and significance was determined via two-tailed one-way ANOVA. NS not significant. **i** Kaplan–Meier survival curves of various groups. A log-rank (Mantel–Cox) test was performed to compare survival between groups ($n = 5$ mice). NS not significant. **j**, **k** Percentages of CD69 + T cells in the CD4+ (**j**) and CD8+ (**k**) T-cell subsets among tumor-infiltrating lymphocytes from different groups ($n = 5$ mice). The data were presented as the mean ± SD; significance was determined via two-tailed Student's *t*-tests. NS not significant. **l**, **m** Proportions of IFN-γ-secreting CD4+ (**l**) and CD8+ (**m**) T cells in the tumor microenvironments of the different groups ($n = 5$ mice). The data were presented as the mean ± SD; significance was determined via two-tailed Student's *t*-tests. NS not significant. **n**, **o** Frequencies of TNF-α-producing CD4+ (**n**) and CD8+ (**o**) T lymphocytes in tumors from different groups ($n = 5$ mice). The data were presented as the mean ± SD; significance was determined via two-tailed Student's *t*-tests. NS not significant. **p** Schematic illustration of the treatment schedule in the mouse model of PDX. **q** The average tumor growth kinetics of PDXs demonstrated different responses to various treatments: PBS, AAV-blank, anti-PD1, AAV (cMSC^{SIPC}), and AAV (cMSC^{SIPC}/CtC^{S}). The tumor volume (mm^3) was monitored daily using a caliper. The data were presented as the mean ± SD ($n = 5$ mice), and significance was determined via two-tailed one-way ANOVA. NS not significant. **r** Kaplan–Meier survival curves of various groups. A log-rank (Mantel–Cox) test was performed to compare survival between groups ($n = 5$ mice). NS not significant.

https://doi.org/10.1038/s41467-025-63377-3

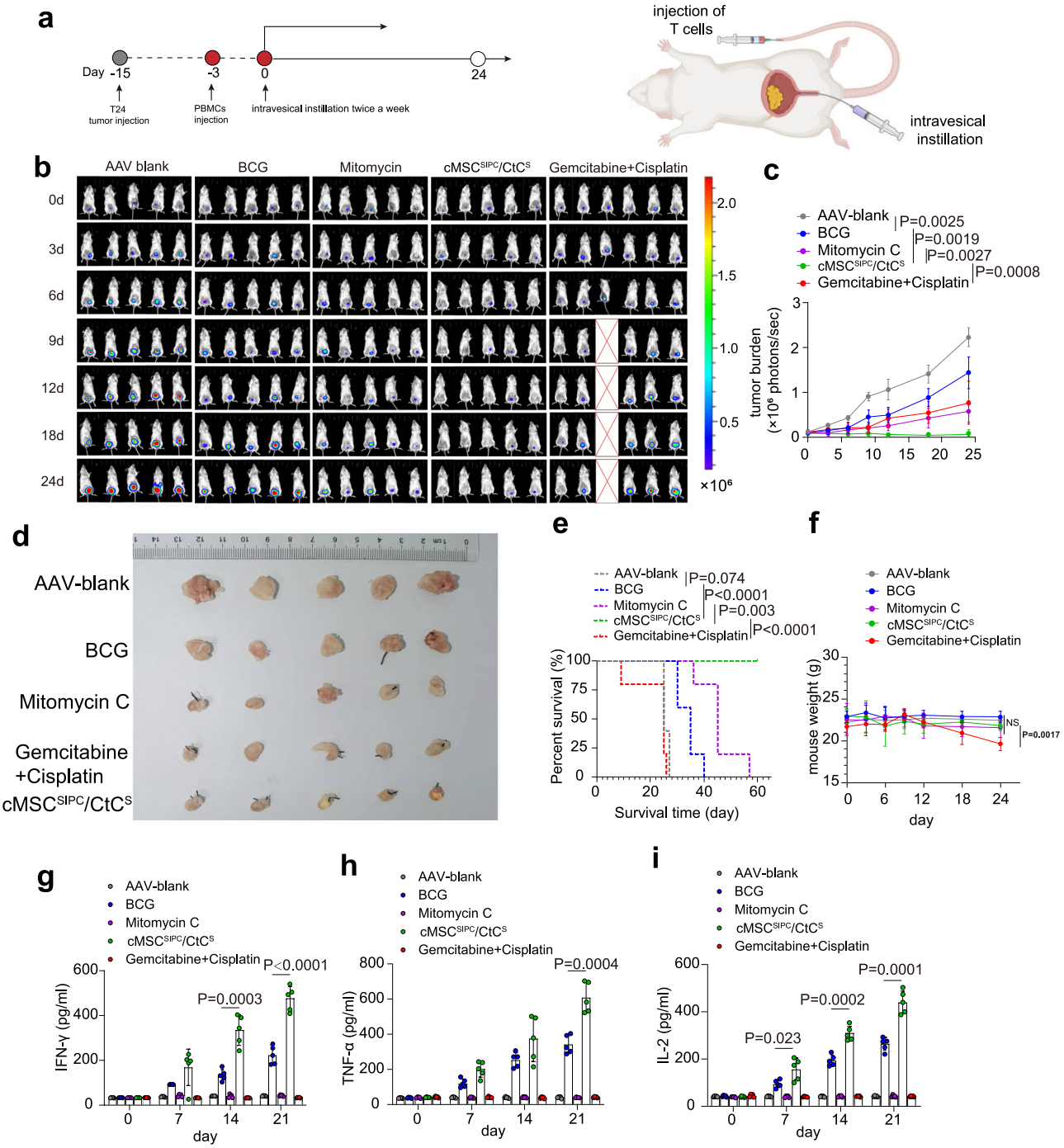

Fig. 6 | Therapeutic efficiency of intravesical instillation of AAV in orthotopic xenograft bladder tumor model mice. a Schematic showing humanized orthotopic murine models of bladder cancer treated with intravesical instillation. Created in BioRender. Zhan, H. (2025) https://BioRender.com/oe2i6ny. **b** In vivo tumor bioluminescence images of each mouse treated with AAV-blank ($n = 5$ mice), BCG ($n = 5$ mice), mitomycin C ($n = 5$ mice), cMSC^{SIPC}/CtC^{S} ($n = 5$ mice), or gemcitabine + cisplatin ($n = 6$) from Day 0 (0 d) to Day 24 (24 d). **c** Tumor burdens of the mice in each group ($n = 5, 5, 5, 5$, and 6 mice per group). The data were presented as the mean ± SD, and significance was determined via two-tailed one-way ANOVA. **d** Representative images of tumors from each group described above. **e** Kaplan–Meier survival curves of various groups. A log-rank (Mantel–Cox) test was performed to compare survival between groups ($n = 5, 5, 5, 5$, and 6 mice per group). **f** Weights of the mice in each group ($n = 5, 5, 5, 5$, and 6 mice per group). The data were presented as the mean ± SD, and significance was determined via two-tailed Student's *t*-tests. NS not significant. **g**–**i** The levels of serum IFN-γ (**g**), TNF-α (**h**), and IL-2 (**i**) in each group ($n = 5, 5, 5, 5$, and 5 mice, respectively) were determined by ELISA on Days 0, 7, 14, and 21. The data were presented as the mean ± SD, and significance was determined via two-tailed Student's *t*-tests. NS not significant.

addressed. First, the validation of the cMSC/CtC platform was focused on models of bladder cancer. The testing of the cMSC/CtC platform will likely need to be performed in various tumor models, more patient-derived tumor cells and a panel of healthy tissues. Second, in theory, the crucial elements of the cMSC/CtC platform are synthesized de novo and have no crosstalk with any endogenous factors of the cells; however, the actual situation is still unknown. Therefore, we should further clarify the long-term specificity and safety of these components in vivo. Third, we demonstrated that only the cMSC/CtC platform drives the expression of multiple immunomodulators to improve the therapeutic effect of cancer immunotherapy. Therefore, future efforts should focus on exploring the effectiveness of more

cMSC/CtC-mediated tumor cell therapy scenarios to demonstrate the universality and modularity of this gene circuit platform.

In conclusion, we constructed an innovative c-MYC-based gene circuit platform for reprogramming cancer cells to trigger specific cancer immunotherapies without the limitations of ITH. Furthermore, our design is modular and can be easily modified to target cancer cells by changing the output gene to express any gene-encoded element, including intracellular, secretory, and cell-surface proteins. In addition, we proposed and validated the efficacy of the cell-to-cell (CtC) system in the treatment of ITH. We characterized c-MYC sensing-based cancer immunotherapy in advanced tumor models and patient-derived tumors, indicating its great potential for clinical application and translation. In further studies, we will optimize the efficacy and safety profile of the cMSC/CtC gene circuit platform for treating other types of tumors. Additionally, we will refine the preclinical evaluation of AAV-mediated cMSC/CtC intravesical therapy for bladder cancer, focusing on both safety and efficacy.

Methods

Ethics

Animal experimentation was approved by the Laboratory Animal Ethics and Use Committee (LAEUC) of Sun Yat-sen Memorial Hospital, Sun Yat-sen University, and was conducted in full compliance with all applicable regulations issued by the Ministry of Science and Technology of the People's Republic of China. The experimental protocols (No. AP20240034 and AP20250057) were reviewed and formally authorized by the LAEUC. All procedures involving tumor-bearing animal models were performed in strict accordance with the approved institutional ethical guidelines.

The human bladder cancer tumor specimen (from a 64-year-old male) was provided by Sun Yat-sen Memorial Hospital, Sun Yat-sen University. The participant has signed a written informed consent form, which includes consent for the publication of clinical information that may identify their identity. This study has been approved by the Ethics Committee of Sun Yat-sen Memorial Hospital, Sun Yat-sen University.

Fresh tumor samples and the paired adjacent normal tissue taken from greater than 2 cm from the tumor obtained from the 30 patients aged from 40 to 80 with bladder cancer who did not receive any neoadjuvant therapeutic intervention at Sun Yat-Sen Memorial Hospital in 2020 and 2022 were collected to perform qRT-PCR for the expression of MUC1 and c-MYC. Among them, 60% patients were males and 40% patients were females. In addition, we collected fresh peripheral venous blood samples from these bladder cancer patients, which were used to isolate peripheral blood mononuclear cells (PBMCs) for in vitro and in vivo experiments in mice. All the participants have signed a written informed consent form. All the fresh tumor samples, the paired adjacent normal tissue and fresh peripheral venous blood samples from these bladder cancer patients used in our research comply with all relevant ethical regulations of the Ethics Committee of Sun Yat-sen Memorial Hospital, Sun Yat-sen University.

All experimental procedures involving patient-derived fresh tumor samples, the paired adjacent normal tissue and fresh peripheral venous blood samples comply with approved institutional ethical guidelines.

Plasmid construction

All the constructs were generated using standard molecular cloning procedures. Vector backbones were linearized by dual restriction enzyme digestion, and DNA fragment inserts were generated by PCR amplification or gBlock de novo synthesis (Integrated DNA Technologies). Both the digestion products and the PCR-generated inserts were resolved on 1% (w/v) agarose gels (Biosharp) supplemented with GelRed™ Nucleic Acid Stain (Yeasen) and electrophoresed at 150 V for 35 min in 1× TAE buffer. The target DNA bands were visualized under ultraviolet light using a SafeImager™ 2.0 transilluminator (Thermo Fisher, G6600) and excised with a sterile scalpel. The gel slices were purified using a DNA Gel Extraction Kit (TIANGEN) according to the manufacturer's protocols. The purified inserts and linearized vectors were ligated by T4 DNA ligase, and in-fusion cloning was performed with a Seamless Cloning Kit. The constructs were subsequently transformed into chemically competent *E. coli* DH5α cells (Weidi), and positive clones were selected on LB agar plates supplemented with the appropriate antibiotic. All the constructs were verified by Sanger sequencing using vector-specific primers. Information on all plasmids is included in Supplementary Data 1. All the RNA inserts were generated by gBlock synthesis (Integrated DNA Technologies), and the DNA sequences used in this study are included in Supplementary Data 2.

Cell line culture and transfection

HEK-293T, U2OS, UMUC3, and COS-7 cells were cultured in DMEM (Gibco®, Life Technologies, Carlsbad, CA), T24 cells were grown in 1640 medium (Gibco®, Life Technologies, Carlsbad, CA), SVHUC1 healthy bladder mucosal epithelial cells were cultured in F12K medium (Gibco®, Life Technologies, Carlsbad, CA), C2C12 myoblasts were maintained in Nutrient Mixture F-12 Ham (DMEM/F-12, Gibco), RWPE-1 cells were cultured in K-SFM medium (Gibco®, Life Technologies, Carlsbad, CA), and iPSC cells were maintained in ExCellerate™ iPSC Expansion Medium (BD Biosciences, San Jose, CA). All types of media were supplemented with 10% (v/v) heat-inactivated FBS and 1% penicillin/streptomycin at 37 °C in 5% CO_2.

For transient transfection experiments, cells were seeded in multiwell plates (Corning® Costar®) 24 h prior to transfection under optimized conditions: 6-well plates at a density of 2×10^5 cells per well in 2 mL of medium, 24-well plates with 5×10^4 cells per well in 1 mL of medium, and 96-well plates containing 1×10^4 cells per well in 200 µL of medium. Transfection was performed when the cells reached 70–80% confluency using Lipofectamine 3000 (Invitrogen) according to the manufacturer's protocol. All subsequent functional assays, including cell manipulations, were performed 48 h after cell transfection, with rigorous implementation of triplicate biological replicates per experimental condition.

Adjustment of c-MYC expression in 293 T cells

We used 293T cells to construct cells stably expressing c-MYC via a tetracycline-on system to control c-MYC expression by adjusting the tetracycline concentration. MYC^{low} indicates cells transfected with 100 nM siRNA for c-MYC, and MYC^{high} indicates cells cocultured with 0.5 µg/ml tetracycline. We modulated the expression level of c-MYC in 293T cells by adjusting the amount of siRNA used and the concentration of tetracycline in the cell culture medium.

Human primary T cells

Human primary T cells were obtained from Sun Yat-sen Memorial Hospital, Sun Yat-sen University (Guangzhou) and cultured in RMPI-1640 supplemented with 10% FBS and 30 units/mL IL-2 (Beijing T&L Biotechnology Co., Ltd.). Human T cells were expanded with Dynabeads® Human T-Activator CD3/CD28 (Gibco®, 11163D). Dynabeads® were added at a bead-to-cell ratio of 1:1. After 3 days of activation, the beads were separated with a magnet, and the cells were cultured for at least one week before they were rested as inactivated and then prepared for cytotoxicity or animal-based assays.

RNAi

Small interfering RNA (siRNA) oligonucleotides and a non-targeting scrambled siRNA control were both synthesized by GenePharma, Shanghai, China and were performed for RNA interference (RNAi) experiments. Transfections were performed using Lipofectamine™ RNAiMAX Transfection Reagent (Thermo Fisher Scientific, Cat#13778030) following the manufacturer's optimized protocols.

Gene silencing efficiency was routinely assessed via quantitative real-time PCR (qRT-PCR) 48 h posttransfection, confirming knockdown of c-MYC expression compared to cells transfected with the scrambled control siRNA. All the specific primers used are listed in Supplementary Data 4.

RNA isolation and qRT-PCR

Total RNA was isolated from cells using TRIzol Reagent (Takara Bio, Cat\# 9109), adhering to the manufacturer's protocol. Briefly, samples were homogenized in TRIzol and phase separation was achieved by the addition of chloroform followed by centrifugation (13,000 × *g*, 15 min). The transparent aqueous phase containing RNA was transferred, and RNA was precipitated by mixing with isopropanol and centrifugation (13,000 × *g*, 10 min). Supernatant was removed carefully and the resulting RNA pellet was washed twice with 75% ethanol (prepared with RNase-free water) followed by centrifugation (7500×*g*, 5 min). RNA was air-dried briefly before being dissolved in RNase-free water. RNA concentration and purity were determined spectrophotometrically using NanoDrop (Thermo Fisher Scientific) by measuring the absorbance ratios at 260/280 nm. Complementary DNA (cDNA) was then synthesized from isolated RNA using the PrimerScript RT-PCR Kit (Vazyme, Cat\# R312-01). Each reverse transcription reaction contained 1 μg of total RNA. Quantitative real-time PCR (qRT-PCR) was performed using the ChamQ Universal SYBR qPCR Master Mix (Vazyme, Cat# Q711-02) on a LightCycler480 Instrument II (Roche). Each reaction mixture contained 1 μL of diluted cDNA, 0.25 μL of 0.5 μM gene-specific forward and reverse primer, 3.5 μL of nuclease-free water and 5 μL of ChamQ Universal SYBR Master Mix. A melt curve analysis was routinely performed at the end of each run to confirm the specificity of amplification. All reactions were performed in technical triplicate for each biological replicate. Cycle threshold (Ct) values were determined using the instrument's software. Relative quantification of target gene mRNA levels was calculated using the comparative $2^{-\Delta\Delta Ct}$ method (Ct, cycle threshold). The mean of Ct values from the housekeeping gene GAPDH was used for normalization.

Exosome extraction

Exosome extraction was performed with a total exosome isolation kit (Invitrogen). In detail, 293T cells were cultured in Dulbecco's Modified Eagle's Medium (DMEM; Gibco) supplemented with 10% exosome-depleted fetal bovine serum (System Biosciences) and transfected with plasmids when they reached 60–70% confluency using Lipofectamine 3000 (Thermo Fisher Scientific) according to the manufacturer's protocol. Six hours posttransfection, the medium was replaced with fresh exosome-depleted complete medium. The cell culture media were collected and thoroughly mixed with the exosome isolation reagents after 48 h of transfection, and the mixtures were incubated at 4 °C overnight. The deposited exosomes were recovered via standard centrifugation (RPM: 10,000×*g*, 60 min). The precipitate was then resuspended in an appropriate amount of PBS. The obtained exosomes could be directly used for subsequent analysis or use. Nanoparticle tracking analysis (NTA) with a NanoSight NS300 instrument (Malvern Panalytical) was performed for size distribution and concentration analysis. For morphological characterization, the exosomes were examined via transmission electron microscopy (TEM).

Single-cell sequence analysis

We collected single-cell transcriptomic data from bladder cancer tumor tissues across ten available datasets (as shown in supplementary Data 4), which included single-cell RNA sequencing data from a total of 69 tumor samples collected from 64 patients with bladder cancer (Supplementary Data 5). During the initial quality control process, we excluded low-quality cells based on the following criteria: (1) < 300 or > 6000 detected genes; (2) < 1000 unique molecular identifiers (UMIs); and (3) > 20% mitochondrial gene counts. To identify and remove potential doublets, we performed doublet removal using doubletFinder. The specific parameter settings were set as follows: pN at 0.25, pK at 0.09, and the expected number of doublets (nExp) was calculated based on the total cell number. Cells identified as doublets by doubletFinder were excluded to ensure the accuracy of subsequent analyses. The filtered count matrix was normalized using the *normalizeData* function in the Seurat R package with default parameters. Next, the *FindVariableFeatures* function was used to identify the top 2000 highly variable genes (HVGs) for further analysis. The data were further scaled and centered using the *ScaleData* function, followed by principal component analysis (PCA). The selection of principal components (PCs) was informed by an evaluation of the elbow and Jackstraw plots. To correct for batch effects, the Harmony algorithm was applied to the PCA-reduced data using the *RunHarmony* function, with the batch key set to "orig.ident". The corrected data were then used to compute cell–cell neighbor relationships, and uniform manifold approximation and projection (UMAP) was implemented on the top 20 Harmony embeddings to visualize cell clustering. Clustering was performed with the *FindClusters* function at a resolution of 1.5 to identify potential cell subpopulations. Cluster annotation was based on the expression of characteristic marker genes for major cell types, including epithelial/tumor cells (EPCAM, KRT18, and KRT19), T/NK cells (CD3D, CD3E, GNLY, and NKG7), B cells (CD79A, CD79B, and MS4A1), myeloid cells (CD14, CSF1R, CD16, and CD68), mast cells (TPSAB1 and TPSB2), fibroblasts (COL1A2, COL3A1, and ACTA2), and endothelial cells (VWF and PECAM1).

ITH description

To assess the intratumoral heterogeneity (ITH) of c-MYC expression in tumor samples, we analyzed the dispersion of c-MYC expression levels at the single-cell level using publicly available single-cell sequencing data. By calculating the entropy of c-MYC expression levels within the cell population, we evaluated the dispersion of expression levels among individual cells in each tumor sample. This approach enabled us to quantify the degree of heterogeneity in c-MYC expression across the tumor cell population.

To calculate the Shannon entropy value (H_{MYC}) of c-MYC based on single-cell sequencing data from a given sample, we assume that the single-cell sequencing dataset for this sample encompasses the c-MYC expression levels (x) across N individual cells: $x = (x_1, x_2 \ldots x_i)$:

(1) Expression normalization:

$$p_i = \frac{x_i}{\sum_{j=1}^{N} x_i}$$

(2) Calculation of the Shannon entropy value:

$$H_{MYC} = -\sum_{i=1}^{N} p_i . \log(p_i)$$

In conclusion, the larger the Shannon entropy value is, the greater the variability in c-MYC expression among individual cells within the single-cell sequencing dataset.

Measurement of ribozyme-regulated gene expression in transiently transfected cells

293T cells were seeded in a 48-well plate and transfected with 25 ng of ribozyme-regulated GFP expression plasmid using Lipofectamine 3000 (Life Technologies) for 24 h. The expression of the GFP reporters was evaluated via flow cytometry to measure the mean fluorescence intensity (MFI). The functional ribozyme activity was calculated as the "fold" inhibition in GFP expression relative to the inactive ribozyme control.

Determining the expression threshold for a c-MYC-activating cMSC

In our study, we analyzed experimental data derived from controlled biological assays that investigated the impact of specific c-MYC activators and c-MYC repressors on our system of interest. To interpret the dynamics of these regulatory elements, we utilized a nonlinear regression approach. Curve fitting and parameter estimation were conducted using the curve_fit function of the SciPy library, leveraging its nonlinear least squares optimization. The initial estimates for the model parameters were chosen based on preliminary experiments and grounded in biological theory. Recognizing the possibility of obtaining biologically implausible values through unconstrained optimization, we instituted strict parameter bounds consistent with the biological nature of the system. The optimization iterated until the algorithm converged, as evidenced by the minimized discrepancy between the model's predictions and the empirical data points. Although the parameters derived from this procedure provided a fit of statistical significance to the measured data, these findings are predicated on the validity of the model's assumption and the reliability of the experimental data.

1. Kinetic model of c-MYC activator-expressing GOIs:

   The function of the c-MYC activator is to increase the activation efficiency of downstream GOIs with increasing c-MYC expression. Based on the kinetic *Hill* equation, we described the effect of c-MYC on the activation efficiency of the c-MYC activator:

$$\frac{dY}{dt} = V_{max} \cdot \frac{X^n}{K_{act}^n + X^n}$$

   where X is the transcription level of the c-MYC activator, Y is the expression of the GOI, V_{max} is the maximum reaction rate, K is the semisaturation constant, and n is the Hill coefficient, which describes the sensitivity of c-MYC activator activity to c-MYC expression.

2. Kinetic model of c-MYC repressor-expressing GOIs:

   The function of the c-MYC repressor is to inhibit the expression efficiency of downstream GOIs by increasing c-MYC expression. Based on the kinetic Hill equation, we described the effect of c-MYC on the inhibition efficiency of the c-MYC repressor on the negative feedback effect:

$$\frac{dY}{dt} = -k \cdot \frac{X}{K_{rep} + X}$$

   where X is the transcription level of the c-MYC repressor, Y is the expression of the GOI, k is the proportionality constant and K is the constant associated with negative feedback.

3. Kinetic model of a cMSC expressing GOIs:

   The kinetic behavior of a cMSC involves the synthesis of a c-MYC activator and c-MYC repressor effects, which can be described as a combination of these two effects. We defined a comprehensive kinetic model that combines the forms of these two Hill equations described above.

$$\frac{dY}{dt} = V_{max} \cdot \frac{X^n}{K_{act}^n + X^n} - k \cdot \frac{X}{K_{rep} + X}$$

where X_{act} and X_{rep} are the transcription levels of the c-MYC activator and c-MYC repressor, respectively; Y is the expression level of the GOI driven by the cMSC; and the other parameters are the same as those defined above.

In vitro cytotoxicity assay

The cytolytic activity of T cells was evaluated using the lactate dehydrogenase (LDH) release assay (Promega, Madison, WI; catalog number G1780) according to the manufacturer's instructions. The percentage of T-cell-mediated cytotoxicity was calculated using the formula: percentage of T-cell-mediated lysis = [(experimental OD value − T-cell spontaneous OD value − test-cell spontaneous OD value)/(test-cell maximum OD value − test-cell spontaneous OD value)] × 100%. Optical density (OD) values obtained from media-only controls were subtracted from all samples prior to analysis.

Enzyme-linked immunosorbent assay (ELISA)

The levels of the IFN-γ, IL-2 and TNF-α proteins secreted into the cell supernatant or mouse plasma were quantified using ELISA kits. The processing steps of the samples to be measured were performed according to the manufacturer's instructions, and the absorbance (OD) at 450 nm was detected in a Cytation 5 luminescence microplate reader (BioTek).

Adeno-associated virus production

To produce cMSC-driven expression viruses, HEK293T cells were seeded at a density of 2×10^6 cells per 15 cm dish and transiently transfected using a triple plasmid transfection system when the cells were at 70–80% confluency. cMSC-driven expression plasmids, AAV serotype plasmids, and pHelper plasmids were cotransfected using a Lipo3000 transfection kit according to the manufacturer's instructions. A total of five dishes were transfected with each AAV. Twenty-four hours after transfection, the cells were harvested in cell culture medium and centrifuged at 4000 rpm for 15 min. The supernatant was discarded, and the cell pellet was resuspended in cell lysis buffer (50 mM Tris-HCl, 150 mM NaCl, 2 mM $MgCl_2$, pH 8.5) and subjected to three freeze–thaw cycles in a dry ice–ethanol bath. The cell lysate was then centrifuged at 4000 rpm for 20 min. To remove the contaminating DNA, benzonase was added to the supernatant, which was subsequently incubated at 37 °C for 30 min. The crude viral preparation was purified via iodixanol density gradient centrifugation. Briefly, the lysate was loaded onto a discontinuous iodixanol gradient (15, 25, 40, and 60%) and centrifuged at 60,000 rpm for 90 min at 18 °C in a Beckman Ti70 rotor. After centrifugation, 3–4 ml of the crude viral mixture was collected from the 40–60% layer with an 18-gauge needle attached to a 10-ml syringe. The crude viral mixture was concentrated to 200–250 µl using an Amicon Ultra15 centrifugal filter (100 kDa), washed once with 8 ml of PBS, and further concentrated to a final volume of 200 µl. Viral titers were quantified by qPCR using primers targeting the AAV ITR region. The cMSC-driven expression viruses were packaged as AAV-2 serotypes, and the final titer of the AAV-2 preparation was $1–2 \times 10^{12}$ genome copies (GC)/ml. Aliquots were stored at −80 °C until use. For in vivo experiments, each mouse was subjected to intravesical instillation or injected intratumorally with 100 µl of AAV solution at a titer of 1×10^9 GC/ml, resulting in a total dose of 1×10^8 GCs per mouse.

Human cancer xenograft mouse model

All the animal studies were conducted with the approval of the Sun Yat-Sen University Institutional Animal Care and Use Committee and were performed in accordance with established guidelines. Immunodeficient NOD.Cg-*Prkdc*scid *Il-2rgtm1 Wjl*/SzJ (NSG) mice, 4–6 weeks of age, were purchased from the Experimental Animal Center of Sun Yat-sen University, housed in SPF barrier facilities and used to perform in vivo assays. The maximal tumor volume permitted by our ethics committee is 1500 mm^3. In our mouse experiments, none of the tumor volumes exceeded the maximum tumor size stipulated by the ethics committee.

To determine the efficiency of target fluorescent protein expression in vivo, mice were subcutaneously injected with 1×10^7 cells (T24 cells or U2OS cells) in the flank. Then, 100 μl AAV suspensions were used for intratumoral injection 10 days after tumor formation. Seven days later, the tumor tissues were harvested for snap-frozen sectioning, and the expression levels of the corresponding fluorescent proteins were observed with a confocal microscope. To validate CtC events in vivo, we generated human xenograft tumor mouse models with T24 cells, and after 10 days of tumor formation, the mice were subjected to intratumoral injection of different groups of AAVs (AAV-GOI and AAV-CtC+AAV-GOI, respectively). Seven days later, the tumors were harvested for snap-frozen sectioning, and the expression of GFP and mCherry was determined by confocal microscopy.

To determine the therapeutic efficiency of AAV-mediated cMSC-driven IFs, NSG mice were subcutaneously injected with 1×10^7 T24 cells or 1×10^7 (RT4-mCherry and RT4-GFP) T24 cells in the flank. When the tumors became visible, their sizes were measured with a digital caliper every 3 days, and the tumor volumes were calculated in square millimeters (length × width^2 × 0.5). After 7 days of tumor formation, human primary T cells were injected intravenously into the tumor-bearing NSG mice, which were set that day as Day 0. AAV vectors were used to encode the expression of various parts of multiple cMSC-driven CIFs, and different AAV suspensions were infiltrated surrounding the tumor via intratumoral injection. Five different AAVs were packaged and used, including a cMSC, to drive bianti-CD3/CD23 scFv expression (AAV1), IL-21 expression (AAV-2), anti-PD1 expression (AAV3), CCL5 expression (AAV4), and CtC component expression (AAV5). Subsequently, intratumoral injections of AAVs were administered to mouse tumors, and the tumor volume was monitored until Day 23. On Days 0, 7, 14, and 21, IFN-γ levels in the mice were measured by ELISA. In the subcutaneous xenograft tumor mouse model, tumor growth was monitored daily using calipers to measure the height × width × length, which was recorded as mm^3. The tumors were resected from the treated human tumor xenograft model and fixed with neutrally buffered 4% formaldehyde, followed by H&E staining.

Humanized orthotopic murine models of bladder cancer

T24 human bladder cancer cells were surgically implanted into the bladders of NSG mice to construct an orthotopic murine model of bladder cancer[52]. After the formation of tumors in the bladder was determined via in vivo fluorescence imaging technology, 1×10^7 nonactivated human primary T cells were injected through the tail veins of the mice to rebuild T-cell immunity, and the day was set as Day 0. The bladders of the mice in each group were instilled with 100 μl of blank AAV suspension, epirubicin (2 mg/ml), or a suspension of cMSC^{SIPC}/CtC^S on Days 0, 3, 6, 9, 12, 15 and 18. On Day 24, we harvested the bladders from all the mice, assessed tumor progression by evaluating bladder size and weight, and used hematoxylin–eosin (H&E)-stained whole bladder sections to determine tumor sizes and the extent of damage to the bladder mucosal epithelium after installation. To determine tumor growth, the mice were injected with 3 mg of VivoGlo Luciferin, in Vivo Grade (Promega; catalog #P1043), 10 min prior to bioluminescence imaging (IVIS spectrum optical imaging system, Xenogen, Alameda, CA). Blood was obtained via facial vein bleeding and spun down at 400×*g* for 10 min to obtain the plasma. The plasma was analyzed using ELISA kits (NOVUS BIOLOGICALS #VAL104) as previously described to quantify the amount of IFN-γ. The resected tumor was paraffin-embedded, and the paraffin sections were incubated at 60 °C for 1 h, deparaffinized and rehydrated with consecutive dilutions of alcohol (95% ethanol, 85% ethanol, and 75% ethanol). The paraffin sections were stained with H&E, followed by analysis using a FISH multifunction scanner (Aperio VERSA 8, Leica).

Patient-derived tumor xenograft construction

Fresh bladder cancer tissues were obtained from consenting patients following surgical resection. After surgical resection, the tumor tissue was kept on ice and processed under sterile conditions. The tissue was washed with PBS, necrotic parts were removed, and the tissue was then cut into 10–20 mm^3 fragments using a razor blade before being stored in sterile DMEM. The fragments were subsequently subcutaneously transplanted into the flanks of the mice through a small skin incision using aseptic surgical techniques. Approximately one month after transplantation, tumor growth was monitored, and the mice were divided into five groups (PBS, AAV-blank, anti-PD1, cMSC^{SIPC} and cMSC^{SIPC}/CtC^S). A total of 1×10^7 nonactivated human primary T cells were injected via the tail vein to reconstitute T-cell immunity. Three days after immune restoration, 100 μl AAV suspensions were intratumorally injected, with the injection day marked as Day 0. For the anti-PD1 group, intraperitoneal administration of the anti-PD1 antibody was initiated on the same day and was repeated every 3 days until the experimental endpoint was reached. The tumor volume was measured weekly using digital calipers. The tumor volumes were calculated in square millimeters (length × width^2 × 0.5).

Bladder cancer and normal urothelium organoid culture

Bladder cancer and normal urothelium organoids were generated and cultured as previously described[53,54]. Fresh bladder cancer tumor and normal urothelium samples were washed three times in PBS supplemented with antibiotics (50 μg/mL nystatin, 500 μg/mL streptomycin, and 500 U/mL penicillin). The tissue fragments were subsequently cut into small particles and incubated with 1 ml of TrypLE for 45 min at 37 °C. The digested suspension was filtered through a 70-μm cell strainer, and the cells were pelleted by centrifugation. The pelleted cells were resuspended in complete culture medium and mixed with Matrigel matrix (BD Biosciences, Cat#356234) at a 1:2 (v/v) ratio. A cell–Matrigel suspension (10,000 cells/30 μL droplet) was plated in 48-well plates and allowed to polymerize. Complete medium was added postpolymerization, followed by culture at 37 °C in a humidified incubator. To determine cMSC effectiveness, when the organoids were ready, we sequentially added the AAV delivering the cMSC-driven expression of GFP into the culture medium and observed GFP expression in the organoid tissue by confocal microscopy after 7 days. For the determination of CtC events in the organoids, we infected the prepared human bladder cancer organoids with different groups of AAVs (AAV-GOI and AAV-CtC+AAV-GOI) to determine the efficacy of the CtC gene therapy model. After 7 days, GFP and RFP expression in the organoid tissue was subsequently assessed by confocal microscopy.

Flow cytometry

(1) Flow cytometry analysis for construct testing:

The cells were seeded in multiwell plates (Corning® Costar®) at a moderate density and were transfected with plasmids when they reached 70–80% confluency. At 48 h posttransfection, the cells were enzymatically trypsinized with 0.25% trypsin-EDTA (Gibco) and centrifuged at 300×*g* for 5 min at 4 °C to remove the supernatant. The cell pellets were resuspended in calcium- and magnesium-free 1× PBS. The median fluorescence intensity and percentage of fluorescence-positive cells were analyzed using a CytoFLEX LX flow cytometer (Beckman Coulter). In our experiments, GFP expression was detected on the FITC channel (488/525 nm), and RFP expression was analyzed on the PE channel (561/585 nm). For each sample, 1×10^5 cells were collected. The cells were initially gated via the forward scatter area (FSC-A) versus the side scatter area (SSC-A) to exclude debris. Subsequent doublet discrimination was achieved through FSC-height (FSC-H) versus

FSC-area (FSC-A) analysis. Data analysis was performed with FlowJo_V10.7 software.

(2) Flow cytometry analysis of immune cells in mouse tumor models:

The mice were euthanized via CO_2 asphyxiation at the experimental endpoint, and the tumors were excised and immediately placed in ice-cold DMEM (Gibco). Tumors were mechanically cut into 1–2 mm^3 fragments using sterile scissors or razor blades, followed by enzymatic digestion in DMEM containing 1 mg/mL collagenase II (Worthington) and 0.1 mg/mL DNase I (Roche) for 45 min in a 37 °C shaker at a gentle speed (200 rpm). The digested suspension was filtered through a 40-μm cell strainer (Corning), centrifuged at 380×*g* for 15 min at 4 °C, and incubated with RBC lysis buffer (BD Pharm Lyse™) for 10 min on ice. After two washes in sterile PBS, the single-cell suspensions were resuspended in PBS and used for flow cytometry staining and analysis. To measure the levels of intracellular cytokines (IFN-γ and TNF-α), the cells were first stimulated with Cell Activation Cocktail (BD Pharmingen) for 6 h at 37 °C under 5% CO_2. The cells were then stained with Fixable Viability Dye for 30 min to exclude dead cells. Surface markers (CD45, CD3, CD4, CD8, and CD69) were detected by staining with fluorochrome-conjugated antibodies (BD Pharmingen) in FACS buffer (PBS + 2% FBS) for 30 min at 4 °C. The cells were then fixed and permeabilized using a Fixation/Permeabilization Kit (BD Pharmingen) according to the manufacturer's instructions. The sections were incubated with the appropriate intracellular antibodies for 45 min at 4 °C in permeabilization buffer. The cells were washed twice with 500 μL of permeabilization buffer and resuspended in 200 μL of PBS. All the antibodies were titrated to optimal concentrations (surface markers: 1:100, intracellular markers: 1:50). Data acquisition was performed with an LSRII Fortessa cytometer (BD Biosciences, San Jose, CA), with 1×10^5 events recorded per sample. The cells were plotted on FSC-A versus SSC-A to gate lymphocytes based on standard light scatter properties. Next, dead cells and doublet exclusion based on FSC-A/SSC-A and viability dye-negative populations were employed. Live single lymphocytes were further gated on CD45+ and CD3+ populations to identify total tumor-infiltrating T cells. CD3 + CD45+ cells were subsequently subdivided into CD4+ and CD8- T cells, CD8+ and CD4- T cells, and CD4- CD8- double-negative events. CD69, TNF-α and IFN-γ expression levels were assessed in both the CD4+ and CD8+ subsets using fluorescence-minus-one (FMO) controls and biological negative controls to set thresholds. CD69+, TNF-α+, and IFN-γ+ positivity within the CD4+ and CD8+ subsets was calculated as a percentage of the parent population. All the detailed information concerning the antibodies used is provided in Supplementary Data 6. Data analysis was performed with FlowJo_V10.7 software.

Immunohistochemistry (IHC)

Tissue samples were obtained from tumor tissues, fixed with 4% paraformaldehyde, embedded in paraffin and cut into 4 μm sections. The slides were incubated at 75 °C for 1.5 h and immersed in fresh xylene for 10 minutes for deparaffinization. The slides were dehydrated with gradient ethanol (100, 95, 85, and 75%) and distilled water. The slides were blocked with 3% BSA for 30 min at room temperature. Antigen retrieval was performed by microwaving the slides in Tris-EDTA buffer (pH 9.0). The sections were incubated with primary antibodies overnight at 4 °C. HRP-conjugated secondary antibodies were then incubated with the sections at room temperature for 30 min. The slides were then stained with 3,3′-diaminobenzidine (DAB) and counterstained with hematoxylin. The slides were mounted for imaging on an optical microscope. All the detailed information concerning the antibodies used is provided in Supplementary Data 6.

Statistics and reproducibility

All experiments were reproduced at least three times, and all attempts at replication were successful, with self-consistent results. Statistical significance was determined by Student's *t*-test (two-tailed) unless otherwise noted. All curve fitting was performed with Prism 8 (GraphPad), and *P* values are reported (not significant NS ($p > 0.05$), $^{*}p < 0.05$, $^{**}p < 0.01$, $^{***}p < 0.001$) and are marked in the figures. All error bars represent the SD. No statistical method was used to predetermine the sample size. No data were excluded from the analyses. The experiments were not randomized. The investigators were not blinded to allocation during the experiments or outcome assessment.

Reporting summary

Further information on research design is available in the Nature Portfolio Reporting Summary linked to this article.

Data availability

Source data are provided with this paper.

References

1. Sharma, P., Hu-Lieskovan, S., Wargo, J. A. & Ribas, A. Primary, adaptive, and acquired resistance to cancer immunotherapy. *Cell* **168**, 707–723 (2017).
2. Spranger, S. Tumor heterogeneity and tumor immunity: a chicken-and-egg problem. *Trends Immunol.* **37**, 349–351 (2016).
3. McGranahan, N. & Swanton, C. Clonal heterogeneity and tumor evolution: past, present, and the future. *Cell* **168**, 613–628 (2017).
4. Rosenthal, R. et al. Neoantigen-directed immune escape in lung cancer evolution. *Nature* **567**, 479–485 (2019).
5. Reuben, A. et al. Genomic and immune heterogeneity are associated with differential responses to therapy in melanoma. *NPJ Genom. Med.* https://doi.org/10.1038/s41525-017-0013-8 (2017).
6. McGranahan, N. et al. Clonal neoantigens elicit T cell immunoreactivity and sensitivity to immune checkpoint blockade. *Science* **351**, 1463–1469 (2016).
7. Vitale, I., Shema, E., Loi, S. & Galluzzi, L. Intratumoral heterogeneity in cancer progression and response to immunotherapy. *Nat. Med.* **27**, 212–224 (2021).
8. Gavish, A. et al. Hallmarks of transcriptional intratumour heterogeneity across a thousand tumours. *Nature* **618**, 598–606 (2023).
9. Quinn, J. J. et al. Single-cell lineages reveal the rates, routes, and drivers of metastasis in cancer xenografts. *Science* https://doi.org/10.1126/science.abc1944 (2021).
10. Liu, C., Kudo, T., Ye, X. & Gascoigne, K. Cell-to-cell variability in Myc dynamics drives transcriptional heterogeneity in cancer cells. *Cell Rep.* **42**, 112401 (2023).
11. Kreuzaler, P. et al. Heterogeneity of Myc expression in breast cancer exposes pharmacological vulnerabilities revealed through executable mechanistic modeling. *Proc. Natl Acad. Sci. USA* **116**, 22399–22408 (2019).
12. Maddipati, R. et al. MYC levels regulate metastatic heterogeneity in pancreatic adenocarcinoma. *Cancer Discov.* **12**, 542–561 (2022).
13. Chen, H., Liu, H. & Qing, G. Targeting oncogenic Myc as a strategy for cancer treatment. *Signal Transduct. Target Ther.* **3**, 5 (2018).
14. Lin, C. Y. et al. Transcriptional amplification in tumor cells with elevated c-Myc. *Cell* **151**, 56–67 (2012).
15. Qin, N. et al. Intratumoral heterogeneity of MYC drives medulloblastoma metastasis and angiogenesis. *Neuro Oncol.* **24**, 1509–1523 (2022).
16. Pongor, L. S. et al. Extrachromosomal DNA amplification contributes to small cell lung cancer heterogeneity and is associated with worse outcomes. *Cancer Discov.* **13**, 928–949 (2023).
17. Butler, D. S. C. et al. A bacterial protease depletes c-MYC and increases survival in mouse models of bladder and colon cancer. *Nat. Biotechnol.* **39**, 754–764 (2021).

18. Speltz, T. E. et al. Targeting MYC with modular synthetic transcriptional repressors derived from bHLH DNA-binding domains. *Nat. Biotechnol.* **41**, 541–551 (2023).
19. Baluapuri, A., Wolf, E. & Eilers, M. Target gene-independent functions of MYC oncoproteins. *Nat. Rev. Mol. Cell Biol.* **21**, 255–267 (2020).
20. Dang, C. V. MYC on the path to cancer. *Cell* **149**, 22–35 (2012).
21. Walz, S. et al. Activation and repression by oncogenic MYC shape tumour-specific gene expression profiles. *Nature* **511**, 483–487 (2014).
22. Finck, A. V., Blanchard, T., Roselle, C. P., Golinelli, G. & June, C. H. Engineered cellular immunotherapies in cancer and beyond. *Nat. Med.* **28**, 678–689 (2022).
23. Wang, Y. et al. Challenges coexist with opportunities: spatial heterogeneity expression of PD-L1 in cancer therapy. *Adv. Sci.* https://doi.org/10.1002/advs.202303175 (2023).
24. Hiam-Galvez, K. J., Allen, B. M. & Spitzer, M. H. Systemic immunity in cancer. *Nat. Rev. Cancer* **21**, 345–359 (2021).
25. Han, H. et al. Small-molecule MYC inhibitors suppress tumor growth and enhance immunotherapy. *Cancer Cell* **36**, 483–497.e415 (2019).
26. Casey, S. C. et al. MYC regulates the antitumor immune response through CD47 and PD-L1. *Science* **352**, 227–231 (2016).
27. Lancet, T. he O. CAR T-cell therapy for solid tumours. *Lancet Oncol.* **22**, 893 (2021).
28. Gauthier, L. et al. Multifunctional natural killer cell engagers targeting NKp46 trigger protective tumor immunity. *Cell* **177**, 1701–1713.e1716 (2019).
29. Ricciuti, B. et al. Genomic and immunophenotypic landscape of acquired resistance to PD-(L)1 blockade in non-small-cell lung cancer. *J. Clin. Oncol.***42**, 1311–1321 (2024).
30. Desbarats, L., Gaubatz, S. & Eilers, M. Discrimination between different E-box-binding proteins at an endogenous target gene of c-myc. *Genes Dev.* **10**, 447–460 (1996).
31. Zhan, H. et al. Multiplexed promoterless gene expression with CRISPReader. *Genome Biol.* **20**, 113 (2019).
32. Wanzel, M., Herold, S. & Eilers, M. Transcriptional repression by Myc. *Trends Cell Biol.* **13**, 146–150 (2003).
33. Yen, L. et al. Exogenous control of mammalian gene expression through modulation of RNA self-cleavage. *Nature* **431**, 471–476 (2004).
34. Zhong, G. et al. A reversible RNA on-switch that controls gene expression of AAV-delivered therapeutics in vivo. *Nat. Biotechnol.* **38**, 169–175 (2020).
35. Martick, M. & Scott, W. G. Tertiary contacts distant from the active site prime a ribozyme for catalysis. *Cell* **126**, 309–320 (2006).
36. Ichikawa, D. M. et al. A universal deep-learning model for zinc finger design enables transcription factor reprogramming. *Nat. Biotechnol.* **41**, 1117–1129 (2023).
37. Simhadri, V. R. et al. Dendritic cells release HLA-B-associated transcript-3 positive exosomes to regulate natural killer function. *PLoS ONE* **3**, e3377 (2008).
38. Alvarez-Erviti, L. et al. Delivery of siRNA to the mouse brain by systemic injection of targeted exosomes. *Nat. Biotechnol.* **29**, 341–345 (2011).
39. Liao, K. W., Lo, Y. C. & Roffler, S. R. Activation of lymphocytes by anti-CD3 single-chain antibody dimers expressed on the plasma membrane of tumor cells. *Gene Ther.* **7**, 339–347 (2000).
40. Liao, K. W. et al. Stable expression of chimeric anti-CD3 receptors on mammalian cells for stimulation of antitumor immunity. *Cancer Gene Ther.* **10**, 779–790 (2003).
41. Nissim, L. et al. Synthetic RNA-based immunomodulatory gene circuits for cancer immunotherapy. *Cell* **171**, 1138–1150.e1115 (2017).
42. Skak, K., Kragh, M., Hausman, D., Smyth, M. J. & Sivakumar, P. V. Interleukin 21: combination strategies for cancer therapy. *Nat. Rev. Drug Discov.* **7**, 231–240 (2008).
43. Lee, J. V. et al. Combinatorial immunotherapies overcome MYC-driven immune evasion in triple negative breast cancer. *Nat. Commun.* **13**, 3671 (2022).
44. Dangaj, D. et al. Cooperation between constitutive and inducible chemokines enables T cell engraftment and immune attack in solid tumors. *Cancer Cell* **35**, 885–900.e810 (2019).
45. Farquhar, K. S. et al. Role of network-mediated stochasticity in mammalian drug resistance. *Nat. Commun.* **10**, 2766 (2019).
46. Guinn, M. T. et al. Observation and control of gene expression noise: barrier crossing analogies between drug resistance and metastasis. *Front. Genet.* **11**, 586726 (2020).
47. Roerden, M. & Spranger, S. Cancer immune evasion, immunoediting and intratumour heterogeneity. *Nat. Rev. Immunol.* **25**, 353–369 (2025).
48. Li, C. & Samulski, R. J. Engineering adeno-associated virus vectors for gene therapy. *Nat. Rev. Genet.* **21**, 255–272 (2020).
49. Russell, S. et al. Efficacy and safety of voretigene neparvovec (AAV2-hRPE65v2) in patients with RPE65-mediated inherited retinal dystrophy: a randomised, controlled, open-label, phase 3 trial. *Lancet* **390**, 849–860 (2017).
50. Strauss, K. A. et al. Onasemnogene abeparvovec for presymptomatic infants with three copies of SMN2 at risk for spinal muscular atrophy: the Phase III SPR1NT trial. *Nat. Med.* **28**, 1390–1397 (2022).
51. Zhang, Q. et al. ETV4 mediated tumor-associated neutrophil infiltration facilitates lymphangiogenesis and lymphatic metastasis of bladder cancer. *Adv. Sci.* **10**, e2205613 (2023).
52. Lorenzatti Hiles, G. et al. A surgical orthotopic approach for studying the invasive progression of human bladder cancer. *Nat. Protoc.* **14**, 738–755 (2019).
53. Hong, X. et al. A HER2-targeted antibody-drug conjugate, RC48-ADC, exerted promising antitumor efficacy and safety with intravesical instillation in preclinical models of bladder cancer. *Adv. Sci.* https://doi.org/10.1002/advs.202302377 (2023).
54. Xie, R. et al. NAT10 drives cisplatin chemoresistance by enhancing ac4C-associated DNA repair in bladder cancer. *Cancer Res.* **83**, 1666–1683 (2023).

Acknowledgements

This study was supported by the National Natural Science Foundation of China (Grant No. 82322056, 82341018, 82072827, 81825016, and 82273421), the National Key Research and Development Program of China (Grant No. 2018YFA0902803), Guangdong Basic and Applied Basic Research Foundation (Grant No. 2021B1515020009), Science and Technology Program of Guangzhou (Grant No. 2023A03J0718, 2024B03J1234, 2024A04J6558, and 202102010002), Fundamental Research Funds for the Central Universities,Sun Yat-sen University (23ykbj002 for Xu Chen), Guangdong Provincial Clinical Research Center for Urological Diseases (2020B1111170006), and Guangdong Science and Technology Department (2020B1212060018, 2018B030317001, and 017B030314026).

Author contributions

H.Z., X.C., and T.L. conceived the study. H.Z., H.W., B.P., and K.X. designed and performed the molecular cloning and cellular biology experiments. H.Z. and H.W. performed the in vivo mouse model experiments and data analysis. K.X., S.C., and H.L. performed the in vitro organoid model experiments. H.Z. and H.W. performed tissue section staining and analysis. J.Lu, J.Lai, and K.J. assisted with PBMC acquisition, adeno-associated virus production and cell culture. H.Z., X.C., H.W., and T.L. wrote the manuscript with input from all the authors.

Competing interests
The authors declare no competing interests.

Additional information
Supplementary information The online version contains supplementary material available at https://doi.org/10.1038/s41467-025-63377-3.

Correspondence and requests for materials should be addressed to Tianxin Lin or Xu Chen.

Peer review information *Nature Communications* thanks Jesus M Paramio, who co-reviewed with Cristian Suárez-Cabrera, and and the other, anonymous, reviewer(s) for their contribution to the peer review of this work. A peer review file is available.